

CHAPTER 4

RESULTS & DISCUSSION

The results and discussions that follow for all parts are included in this chapter. This chapter discusses the results of Part 1 as TG/DTA analysis of all fluxes, macro- and micro-observation of the magnesium surface layer, and study of the influence of fluxes on the mechanical properties of magnesium. Results of manganese recovery from various Mn sources are discussed. The role of temperatures is also considered for checking the Mn recovery. The effects of manganese, copper and nickel in magnesium were investigated in terms of the microstructure changes, variation in mechanical properties and corrosion behaviour. This chapter included all of the findings and comparative analyses for the Mg-Mn, Mg-Cu, Mg-Cu-Mn, Mg-Ni, and Mg-Ni-Mn systems.

4.1 Raw Materials Analysis

Chemical analysis of raw material was carried out by JEOL JSM-5610LV Energy Dispersive Spectroscopy (EDS) and the data were analyzed by Oxford software. The accuracy of the instrument is 99.99 wt. %. Raw materials are divided into three parts.

- 1) Metals: Magnesium, Manganese, Copper, Nickel
- 2) Manganese sources (powder): Mn coarse powder, MnCl₂, MnO₂, Mn fine powder
- 3) Chemicals used for fluxes: MnCl₂, CaF₂, MgO, KCl, CaCl₂, BaCl₂, MgCl₂, NaCl

Chemical composition of the all-raw materials is shown in table 4.1.

Table 4.1 EDS analysis of raw material

Metals					
	Mg	Mn	Cu	Ni	O
Magnesium	98.68	0.08	-	-	1.24
Manganese	-	99.12	-	-	0.88
Copper	-	-	98.93	-	1.03
Nickel	-	-	-	98.80	1.2
Different Mn forms (powder)					
	Mn	O	Cl	Other	
Mn coarse powder	82.16	13.28	-	4.56	

MnCl ₂ .4H ₂ O (before drying)	39.26	13.66	47.08	-	-	-	-	-	-
MnO ₂	61.78	34.61	-	-	-	-	-	-	-
Mn fine powder	61.67	35.67	-	-	-	-	-	-	2.67
Chemicals used for fluxes									
	Ba	Mn	Cl	Ca	Mg	O	Na	F	K
BaCl ₂	67.37	0.10	32.52	-	-	-	-	-	-
CaCl ₂	-	-	47.36	22.25	0.47	29.92	-	-	-
MgCl ₂ .6H ₂ O	-	-	38.87	-	13.36	47.77	-	-	-
KCl	-	-	42.22	-	-	18.04	6.07	-	33.67
MnCl ₂ .4H ₂ O	-	39.26	47.08	-	-	13.66	-	-	-
NaCl	-	-	61.81	-	-	-	38.19	-	-
MgO	-	-	-	-	43.72	56.28	-	-	-
CaF ₂	-	-	-	47.01	-	-	-	52.99	-

X-ray diffraction analysis of pure magnesium was carried out in Pan analytical (X'Pert Pro) system. The XRD pattern & 2 θ , d value, present phases and JCPDS card reference no. is shown in figure 4.1 and table 4.2 respectively.

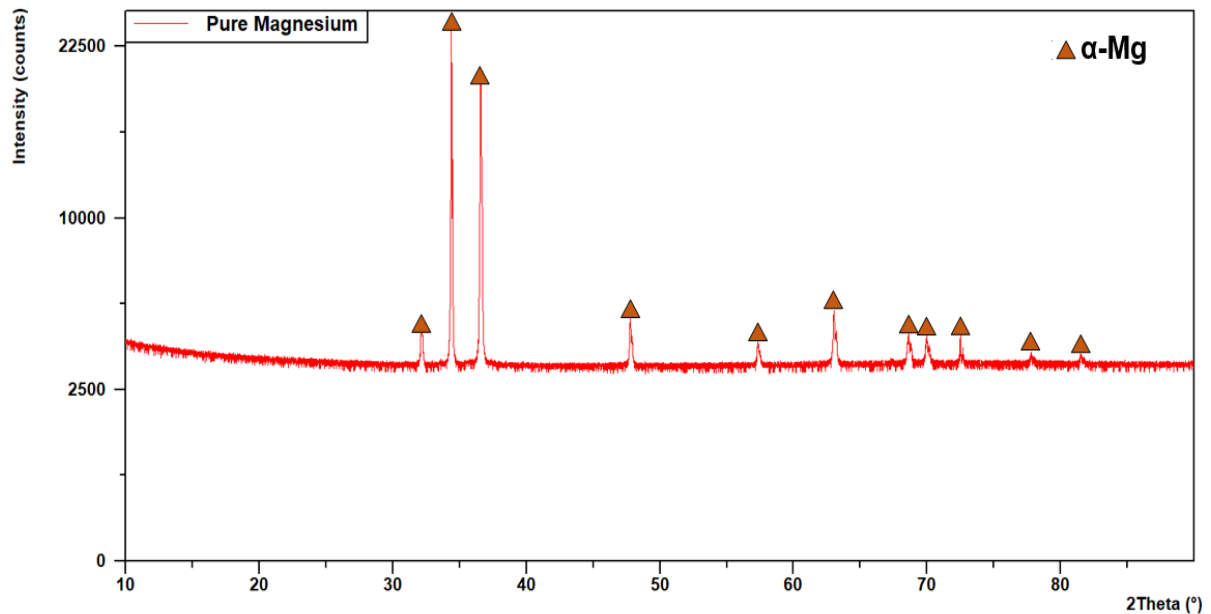


Figure 4.1 XRD Pattern of pure magnesium

Table 4.2 Standard and Experimental XRD values of pure magnesium

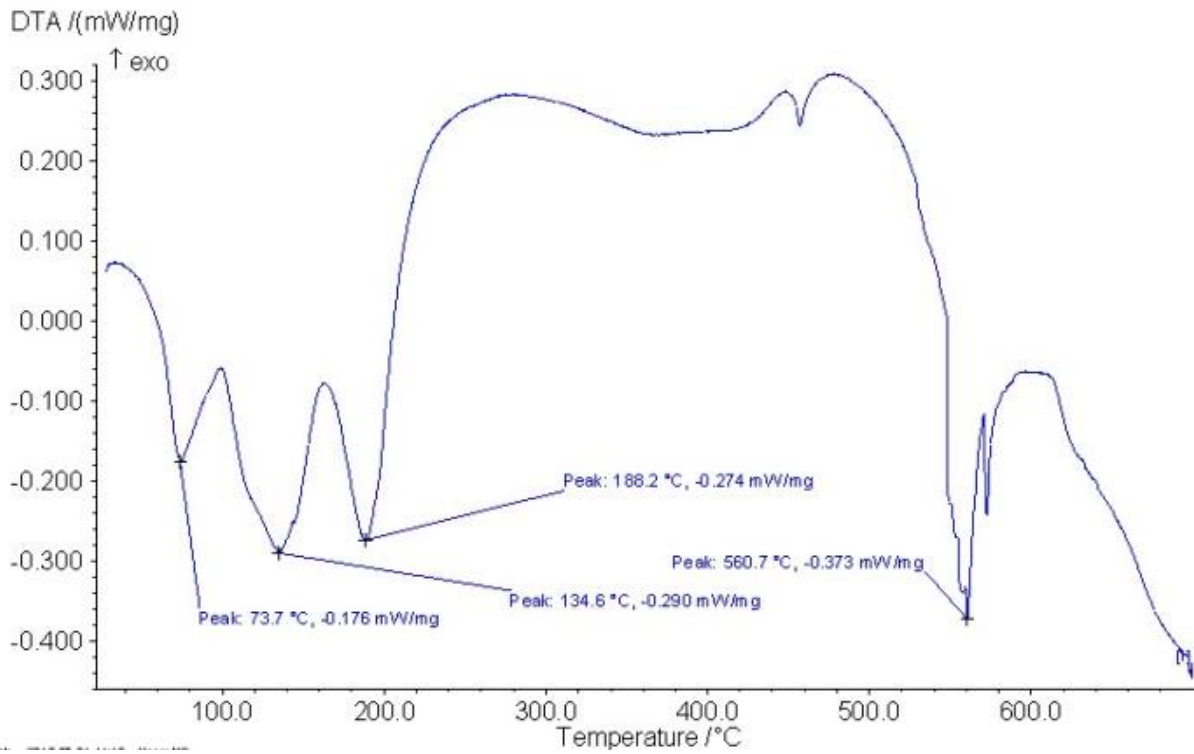
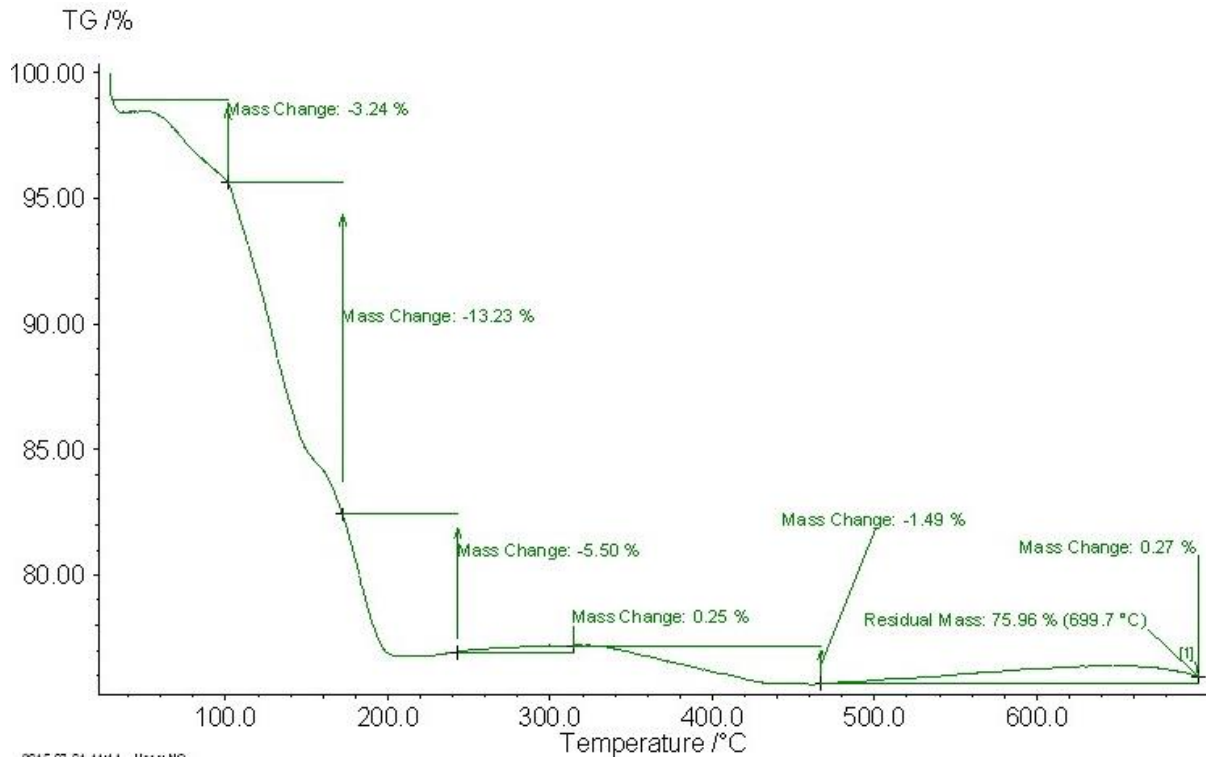
Sr. No.	Pos. (Experimental) [$^{\circ}2\theta$.]	d-spacing (Experimental) [\AA]	d-spacing (Standard) [\AA]	Phase	Reference No.
1	32.1453	2.78461	2.780	α -Mg	4-770
2	34.4722	2.60610	2.606		
3	36.6819	2.45403	2.453		
4	47.9124	1.90182	1.901		
5	57.3370	1.60566	1.605		
6	63.2173	1.47337	1.473		
7	68.8215	1.36645	1.366		
8	69.9765	1.34337	1.343		
9	72.4858	1.30292	1.303		
10	77.7796	1.22693	1.227		
11	81.5054	1.18000	1.1795		

4.2 Results & Discussion of Part I

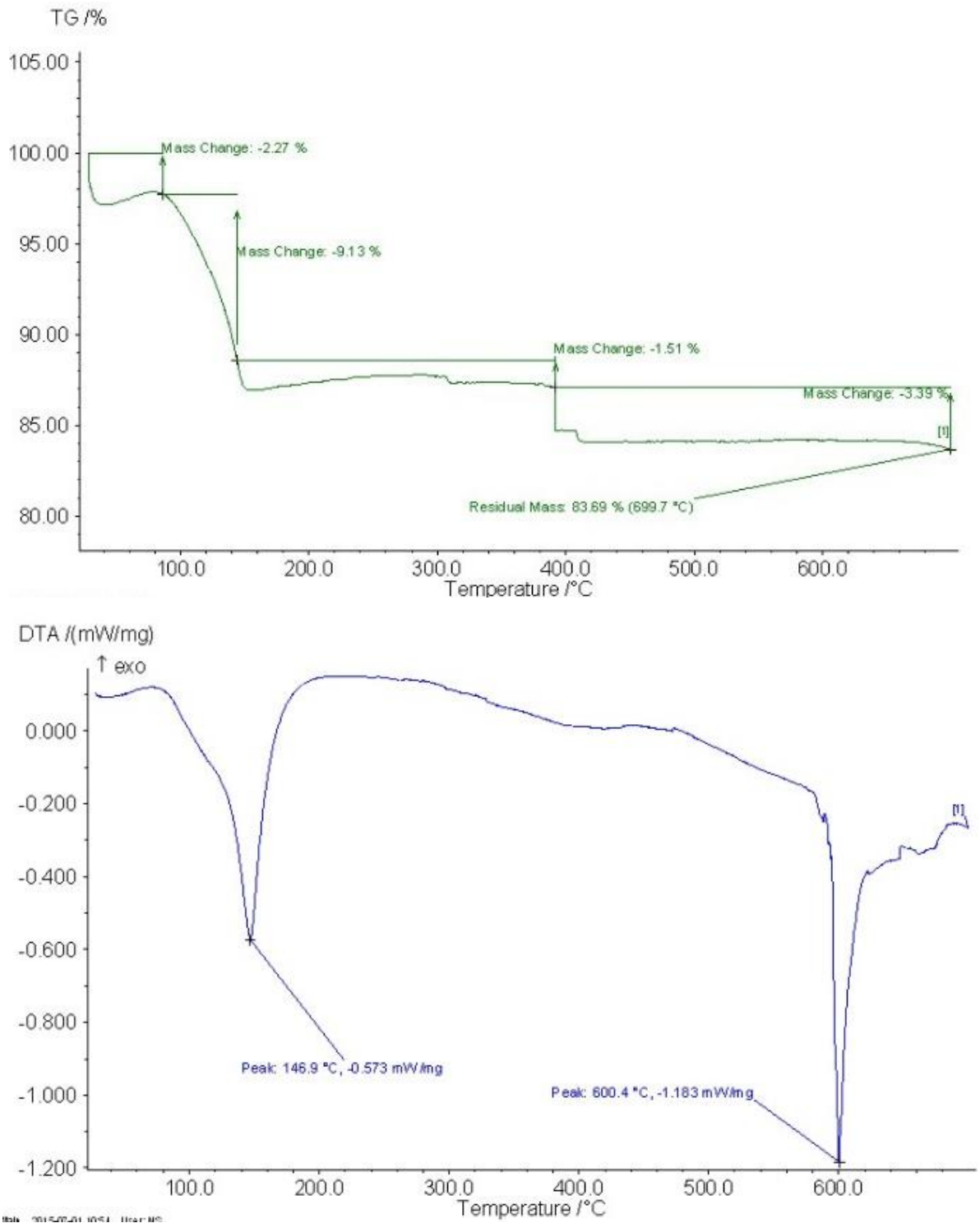
Develop the Magnesium Melting Fluxes and Identify the Best Among Them

4.2.1 Thermogravimetric/Differential Thermal Analysis of All Fluxes

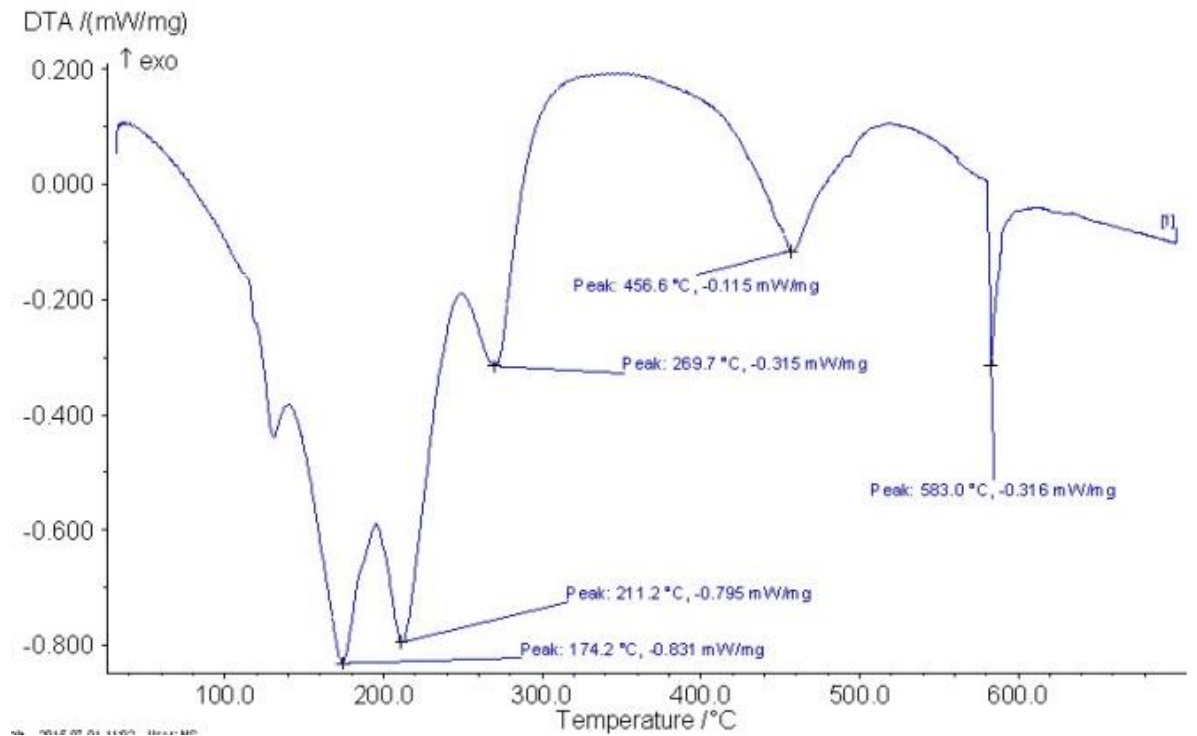
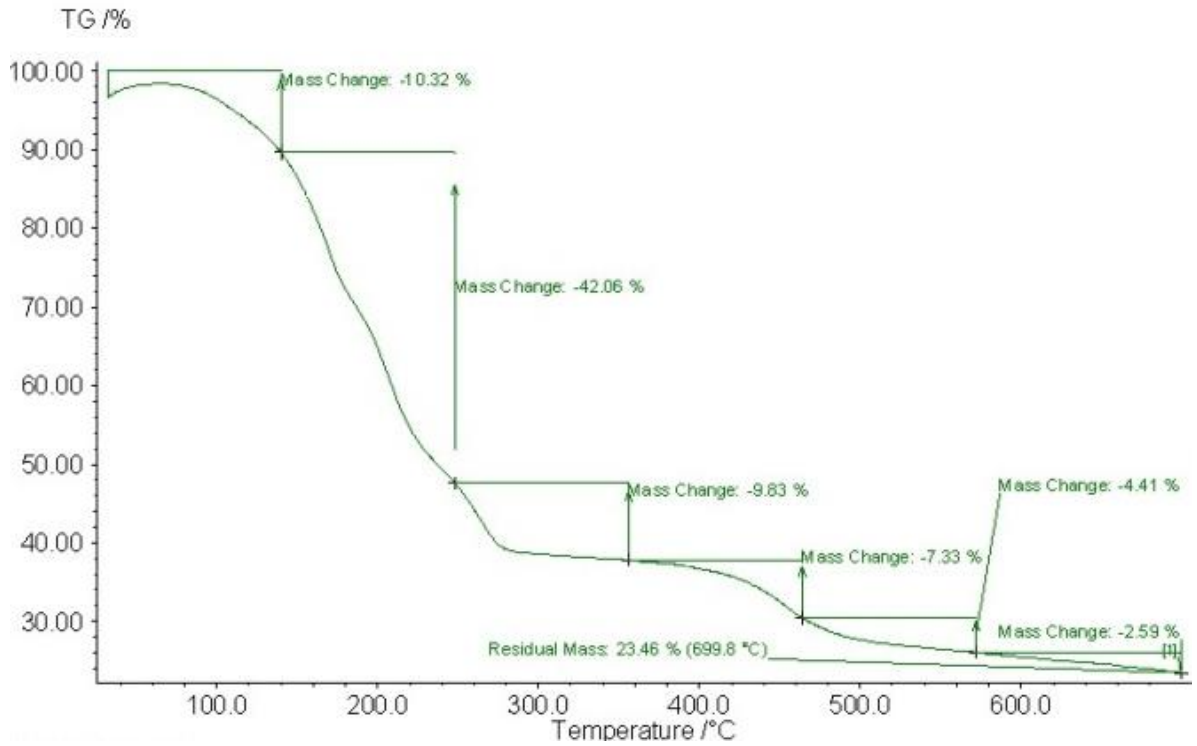
To melt the flux before the actual melting of solid magnesium metal, a proper combination of chemicals (salts) is very important. Not only that, but flux also had to start reducing the diffusion of oxygen on the surface of the semisolid charge to avoid fires. According to the ternary diagram of three chlorides like MgCl_2 , KCl and NaCl , the melting behavior start at 385°C - 500°C . [126] During present study, nine types of fluxes were prepared by varying the amount of MgCl_2 , KCl , CaCl_2 , BaCl_2 , NaCl , MgO and CaF_2 . Only one type of fluoride is used to improve the wettability problems of the MgCl_2 . By varying the amount of chemicals (salts), the melting behavior of the fluxes changed. Therefore, to understand fluxes behavior, thermal analysis has been carried out and it is reported in figure 4.2. Thermogravimetric/Differential Thermal Analysis graphs indicate the mass change (%) and decomposition temperature of fluxes at different stages.



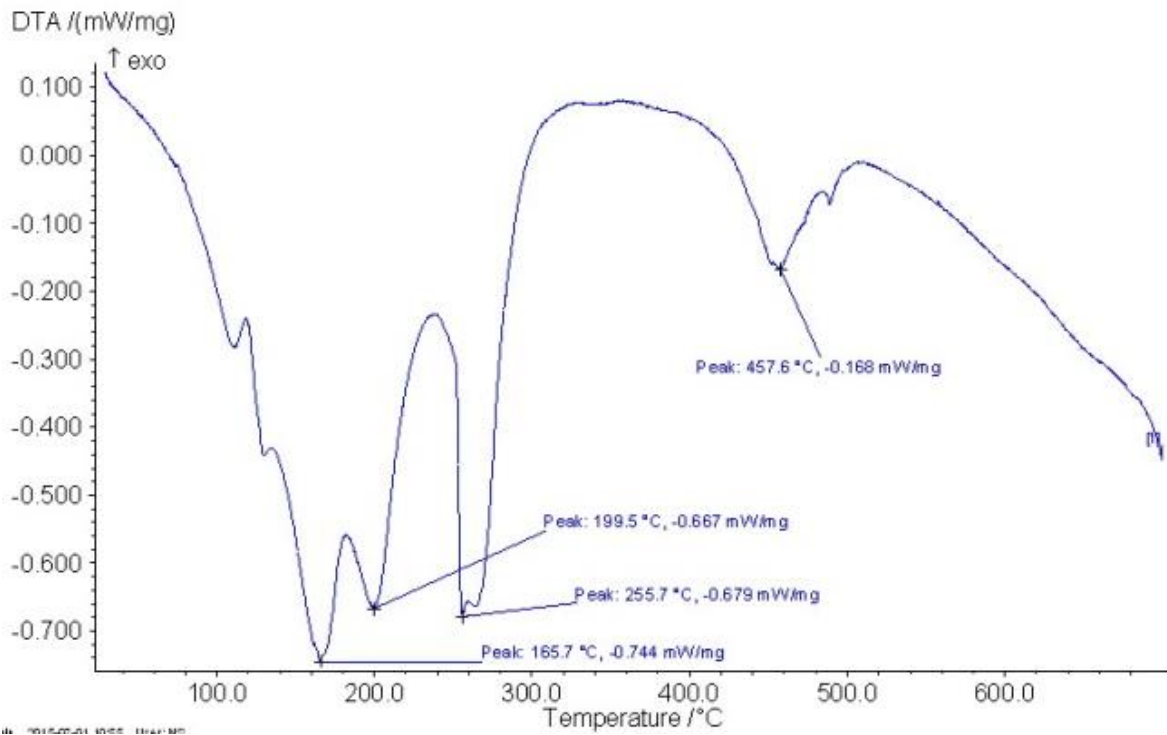
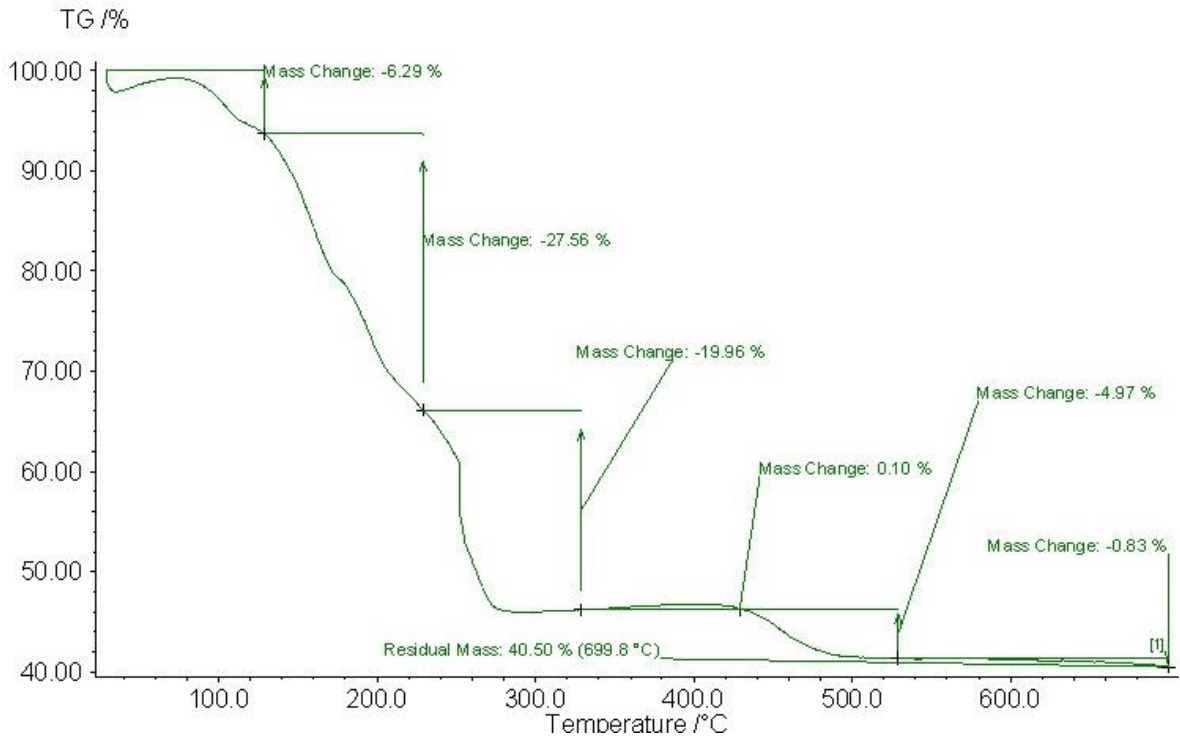
(a) Flux 1 (320)



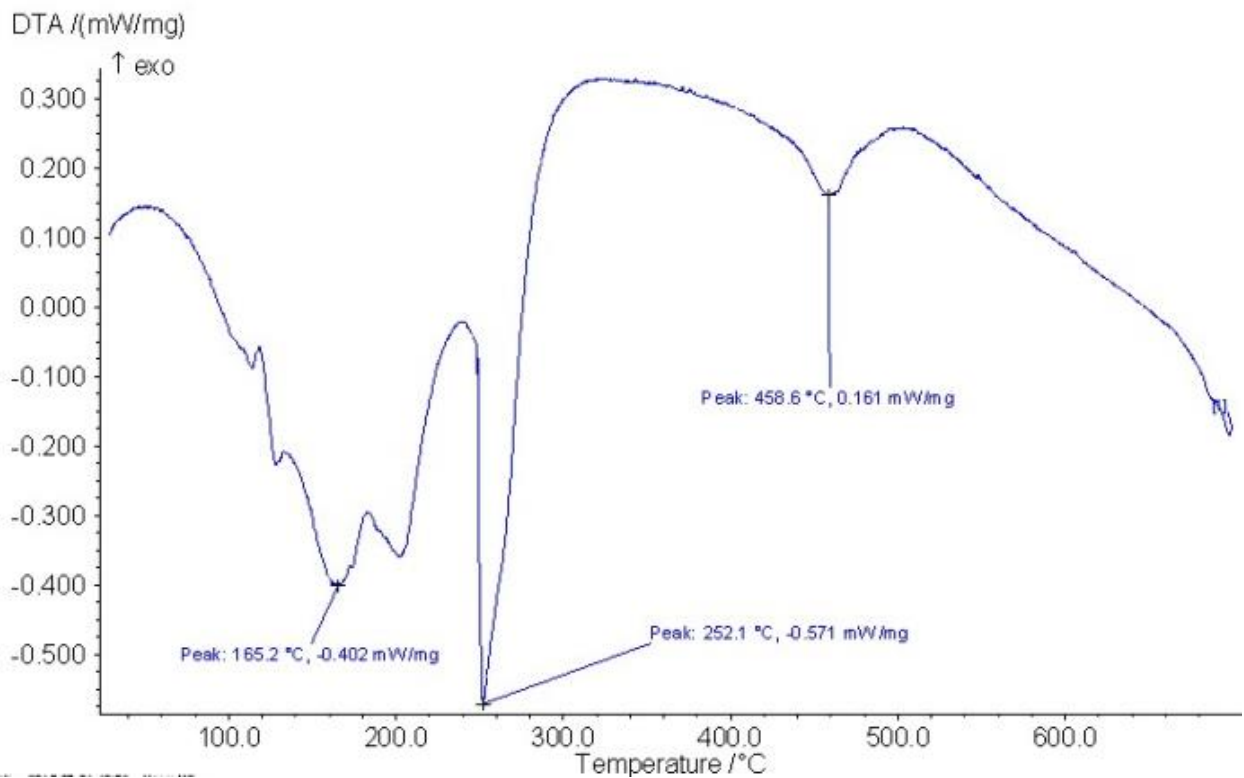
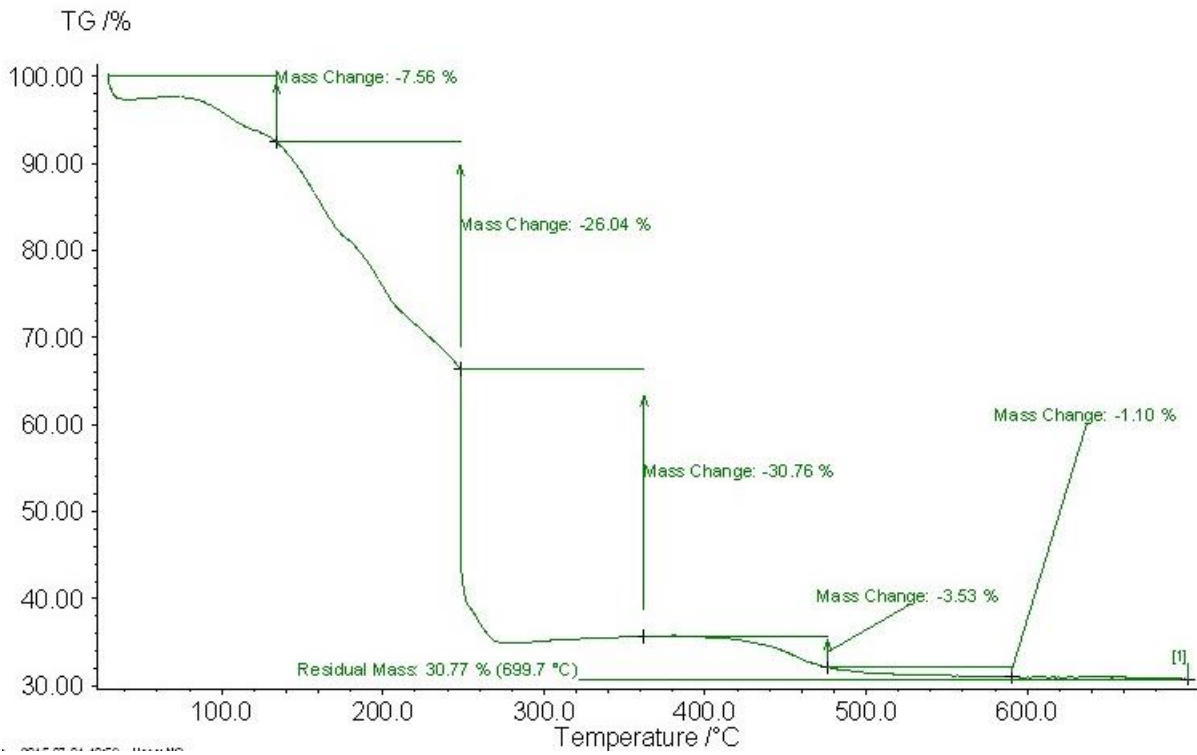
(b) Flux 2 (220)



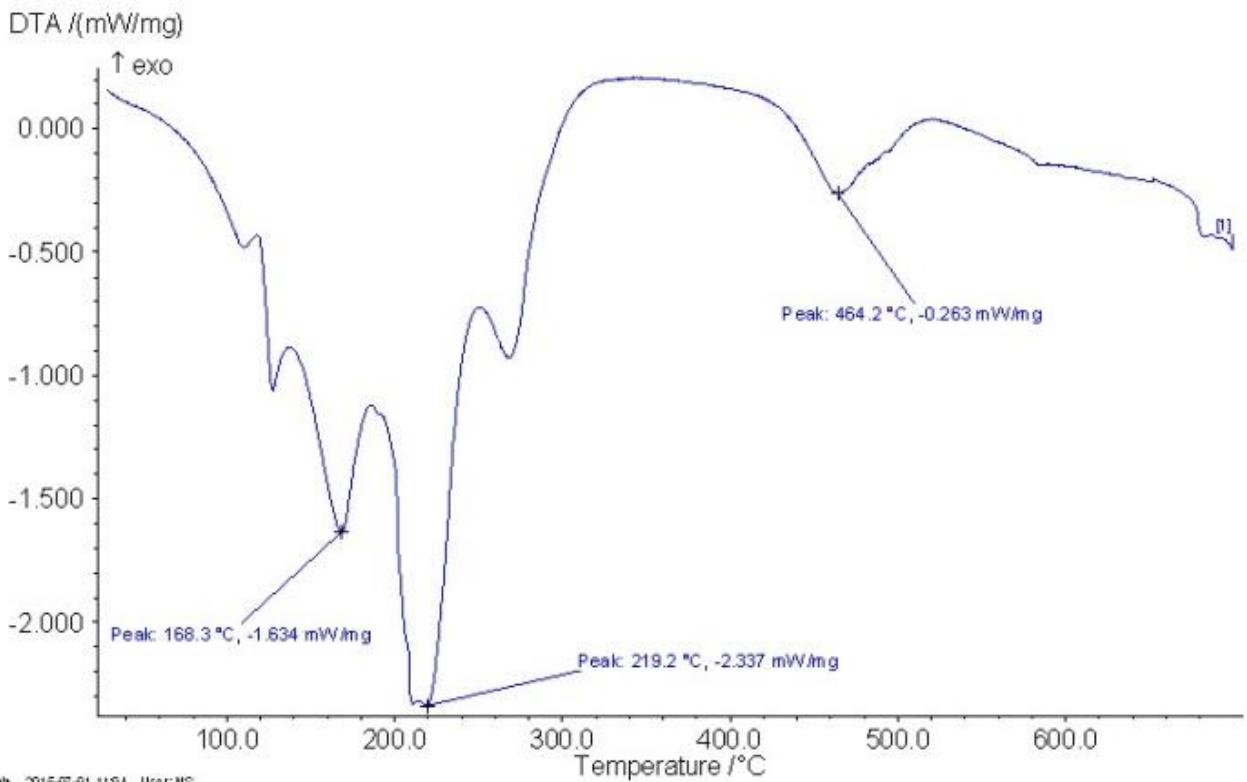
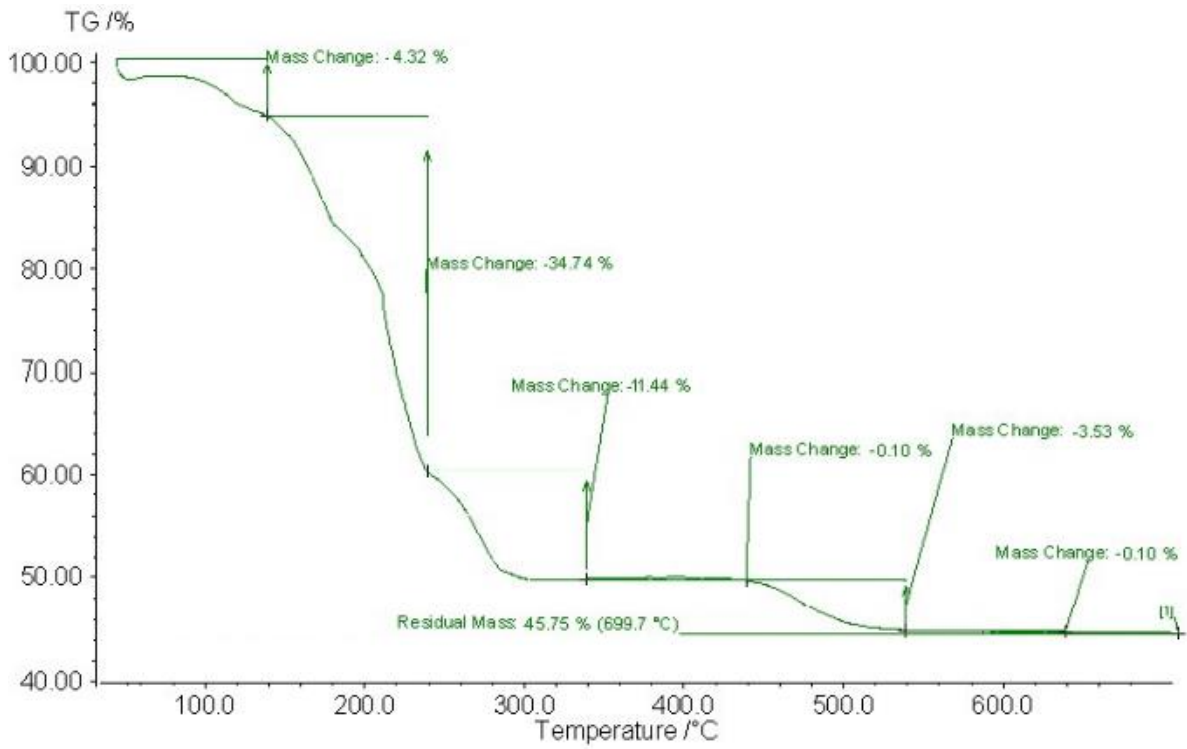
(c) Flux 3



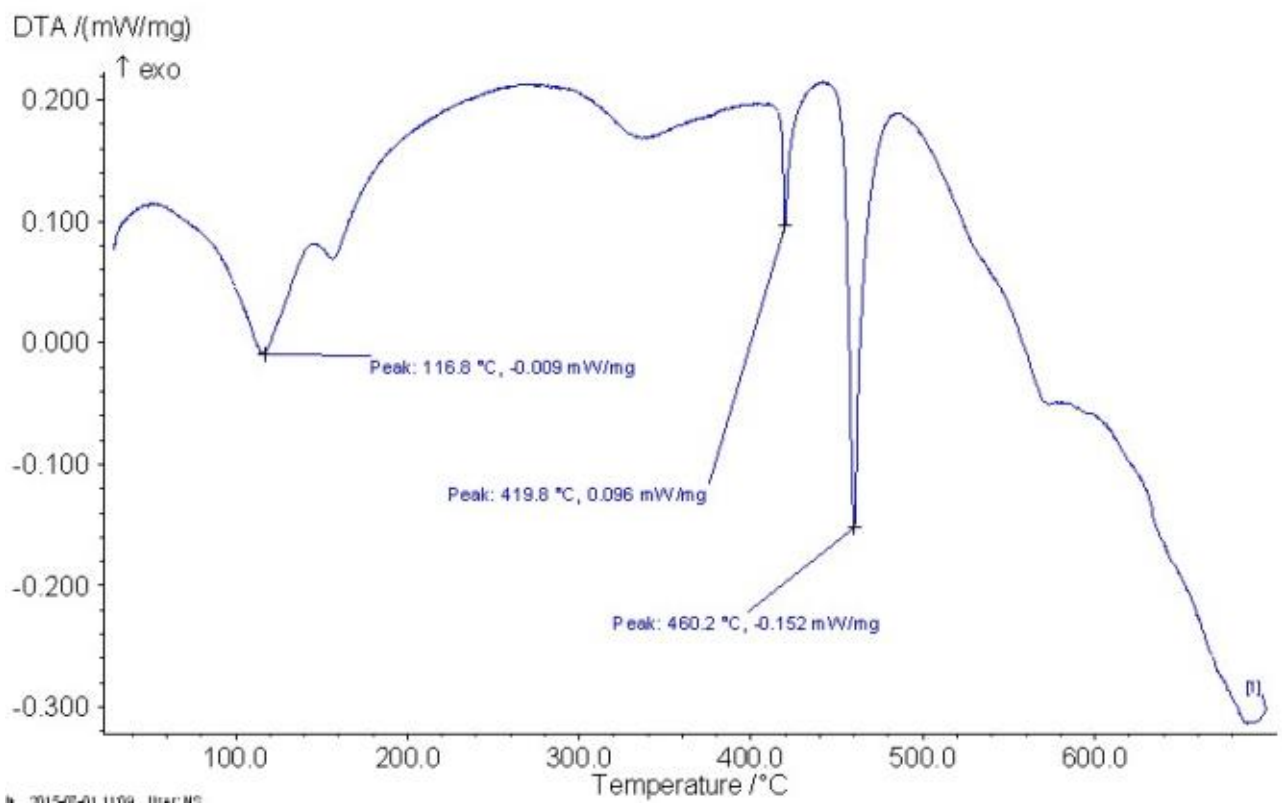
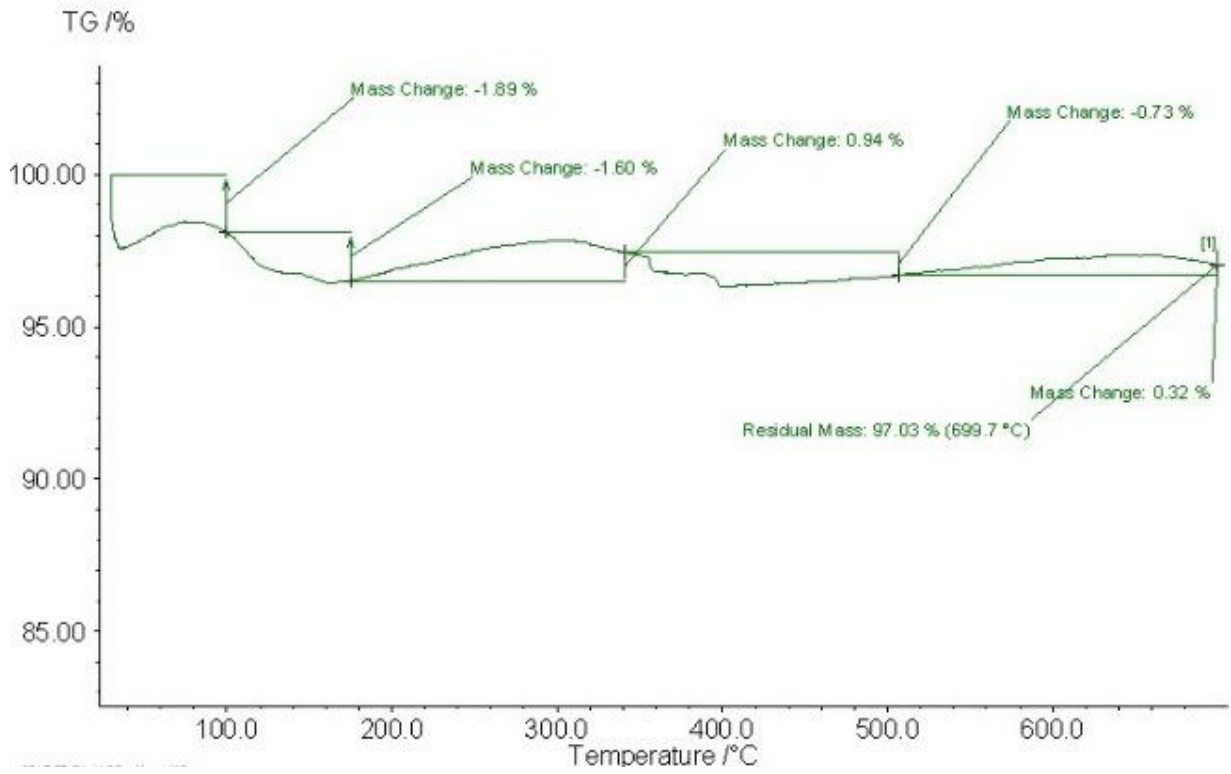
(d) Flux 4 (230)



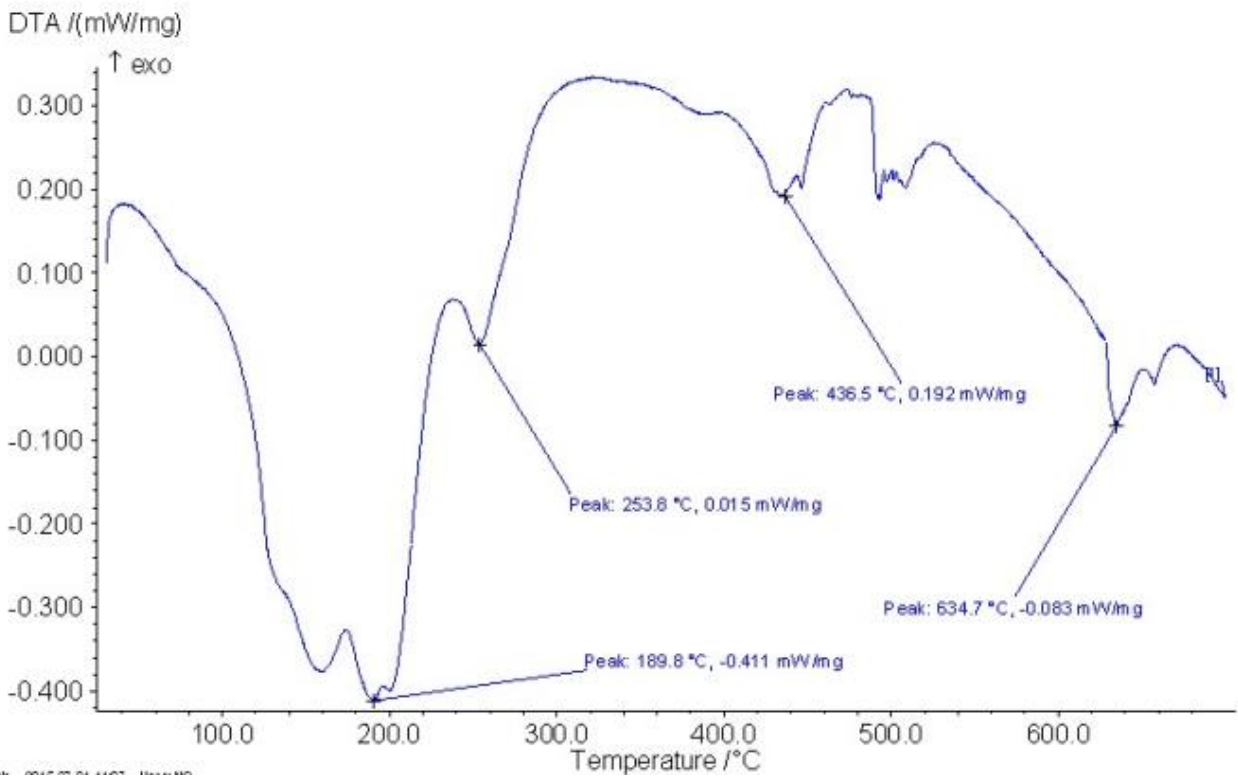
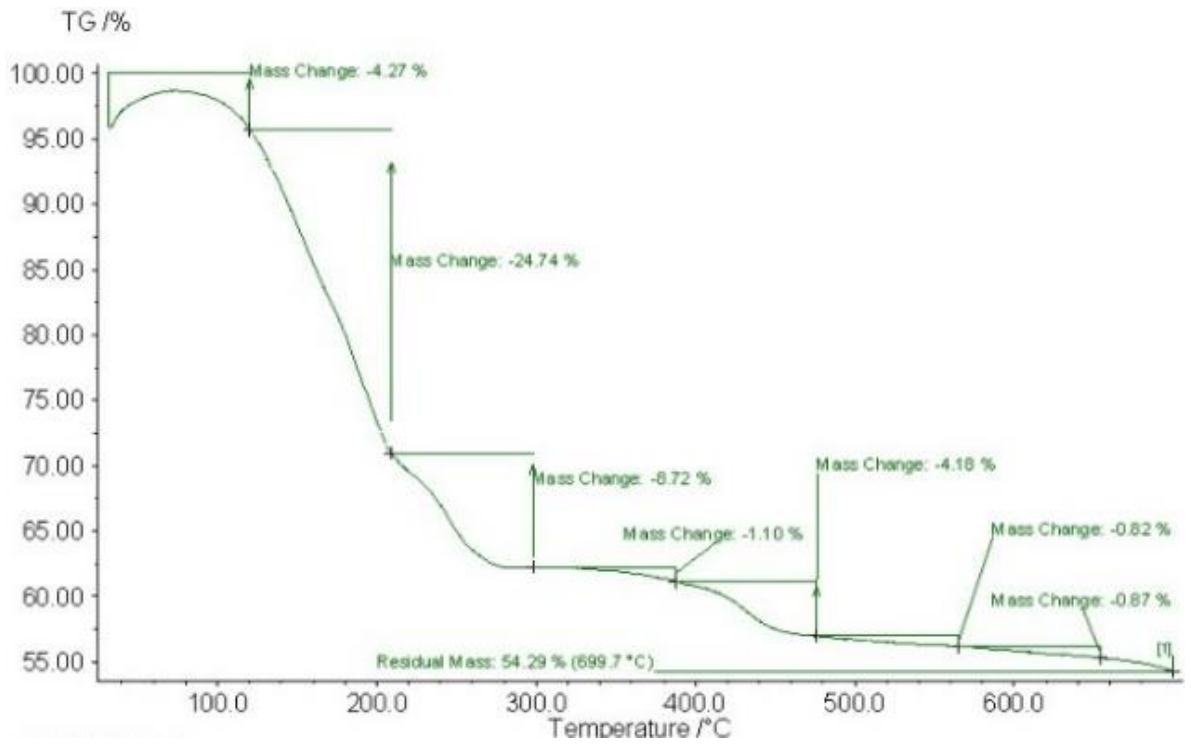
(e) Flux 5 (310)



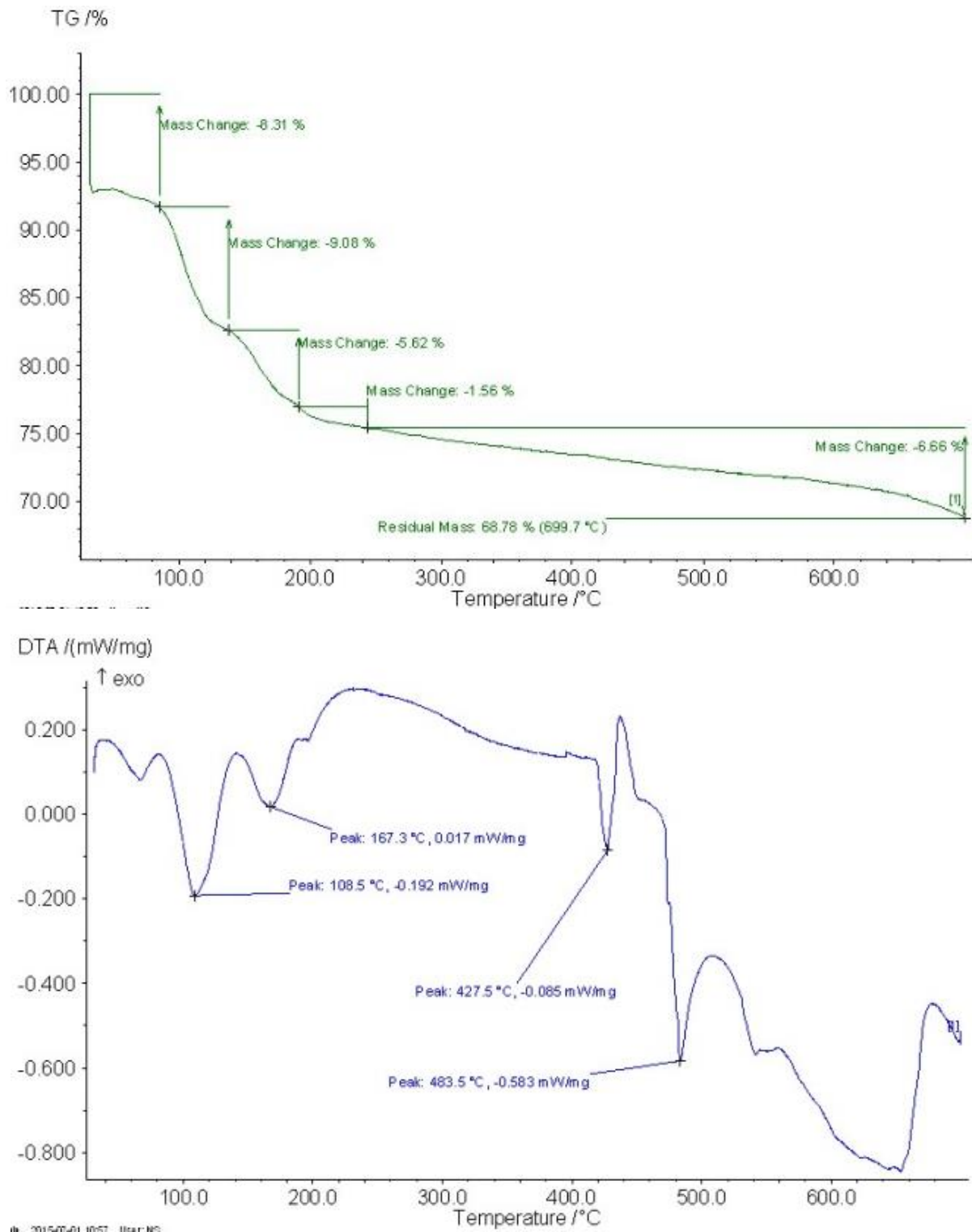
(f) Flux 6



(g) Flux 7



(h) Flux 8

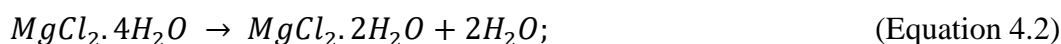
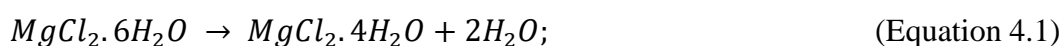


(i) Flux 9 (250)

Figure 4.2 TG/DT analyses of all fluxes

As shown in figure 4.2(a), flux 1 decomposed at 560.7 °C temperature. DTA of Flux 1 shows three endothermic peaks at 73.7 °C, 134.6 °C, and 188.2 °C. TG graph of flux 1 shows,

multistage decomposition. Around 22% of flux mass is reduced up to 250 °C due to the removal of chemically bounded water and volatile matter present in the flux. 75.96 % residual flux is present at around 700 °C. The decomposition temperature of flux 2 is 600.4 °C presented in figure 4.2 (b). Physically bounded water present in barium chloride is released at 146.9 °C and 11.4% mass of flux is decreased at this stage. Magnesium chloride-containing fluxes like flux 3, 4, 5, 6, and 8 shows nearly a similar pattern in the DTA graph up to 250 °C temperature which is shown in figure 4.2 (c), (d), (e), (f) and (h). Moisture present in hydrous magnesium chloride is driven off step by step in all 5 fluxes (Fig. 4.2 c, d, e, f, and h) and it is removed by the following reactions: [132]



DTA of flux 3 shows, sharp endothermic peak (melting) at 583 °C, and around 73.95 % mass change occurs at this temperature. DTA of flux 4 shows two endothermic peaks at 450 °C to 540 °C which represents its melting point. Flux 5 and 6 are melted at 458.6 °C and 464.2 °C respectively. Flux 8 contains the majority of chloride and 1.5 % oxide. Flux 8 shows two endothermic peaks at 436.5 °C and 634.7 °C temperatures represent its decomposition. Due to the presence of a maximum percentage of chlorides and 16% calcium fluorides, two sharp endothermic peaks are observed at 419.8 °C and 460.2 °C in flux 7 (Fig. 4.2 g) compared to flux 8 (Fig. 4.2 h). Flux 9 contains 72 % manganese chloride, 23 % potassium chloride, and a minor amount of barium chloride and calcium fluoride.

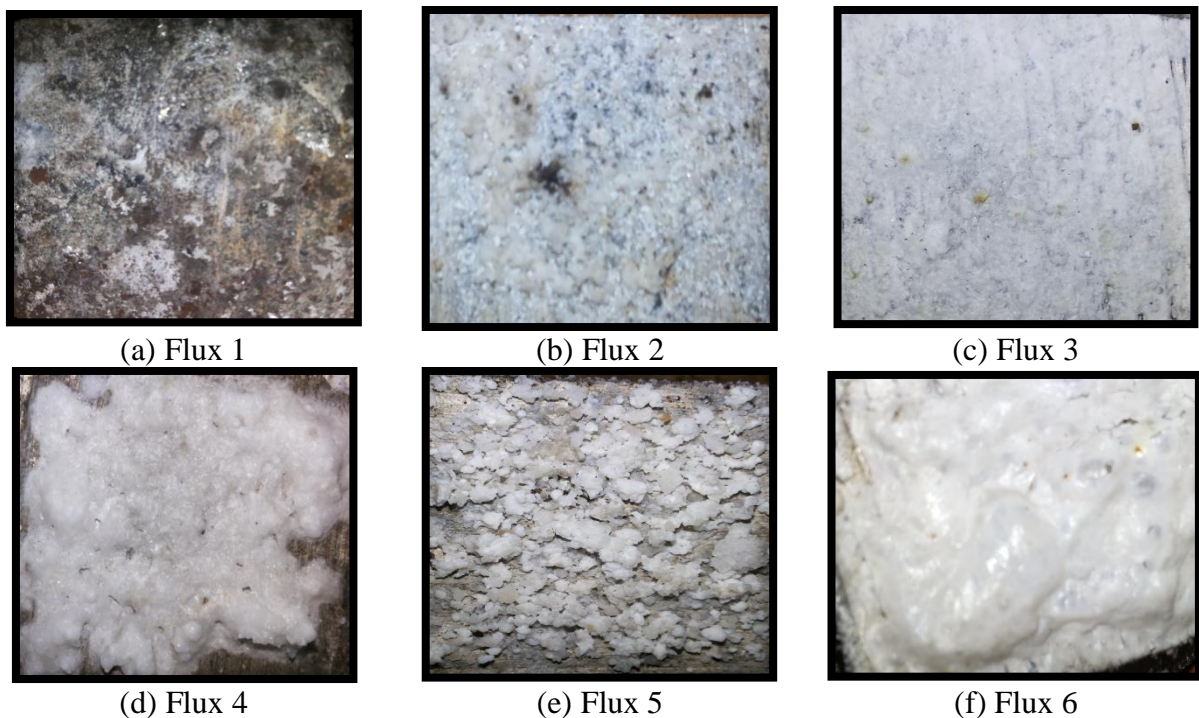
The decomposition of this flux starts at 427.5 °C and continues up to 483.5 °C (Fig. 4.2 I). The volatile matter was removed before 200 °C in this flux. 25 % to 40 % mass change is observed in the TGA graph of flux 4, 5, 6, 8, and 9 up to 250 °C temperature. In the case of flux 7, 3.49 % of mass reduction is observed due to the presence of more % of CaF₂ and the absence of BaCl₂ till 250 °C temperature. At around 700 °C temperature, 97.03% residual mass is present in flux 7 which is highest compared to other fluxes.

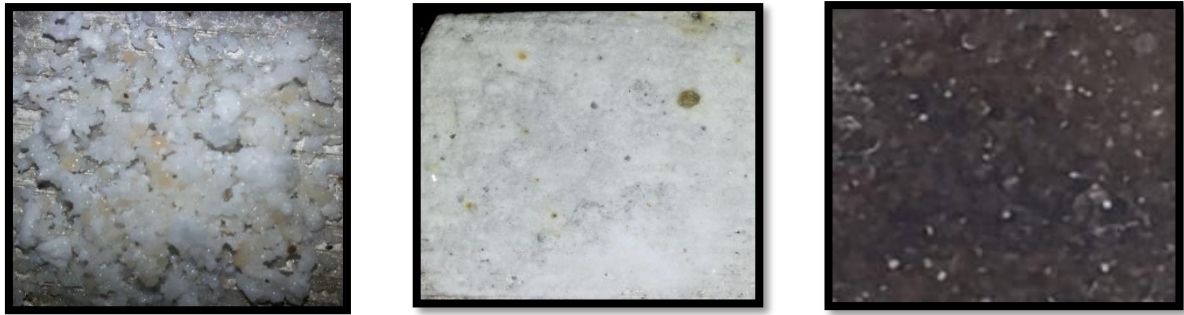
All thermal analysis results indicate that the proper covering layer of fluxes was started before the actual melting of magnesium metal. Thus, magnesium melting can be possible by

using a different flux, but the amount of magnesium metal recovery varies from flux to flux. The present research work focuses on magnesium melting because once the burning of molten magnesium is controlled then alloying can be possible. Moreover, magnesium alloys like AZ series, AM series,[133], Mg-Zn alloy[134], Mg-Mn alloy [135], Mg-Mn-Sn, Mg-Bi[136], Mg-Mn-Cu, Mg-Mn-Ni, etc. were also prepared by using these fluxes.

4.2.2 Observation of Surface Layer of Flux on Magnesium

Figure 4.3 indicates a micrograph of a fused flux layer on a solid magnesium surface at 10X magnification. Figure 4.4 indicates a scanning electron micrograph at 100 X magnification. It is observed that flux 1 generates a thick layer due to the presence of magnesium oxide. As shown in figure 4.3 (b, c), flux 2 and 3 create a smooth layer on the magnesium surface. However, SEM image of them indicates the formation of small cracks (Fig. 4.4 b, c). Due to these cracks formation, oxygen entrapment chances are more so, it can affect the % yield of the final metal (magnesium). Flux 4 and 6 generate a porous layer along with the formation of bubbles and cracks on the surface. Flux 5 and 7 are fused on the surface and create a lumpy layer, which means some flux particles are fused and the remaining are non-fused at this stage. Flux 8 and 9 generate a smooth and adherent layer on the magnesium surface which protects the solid magnesium metal piece before actual melting.



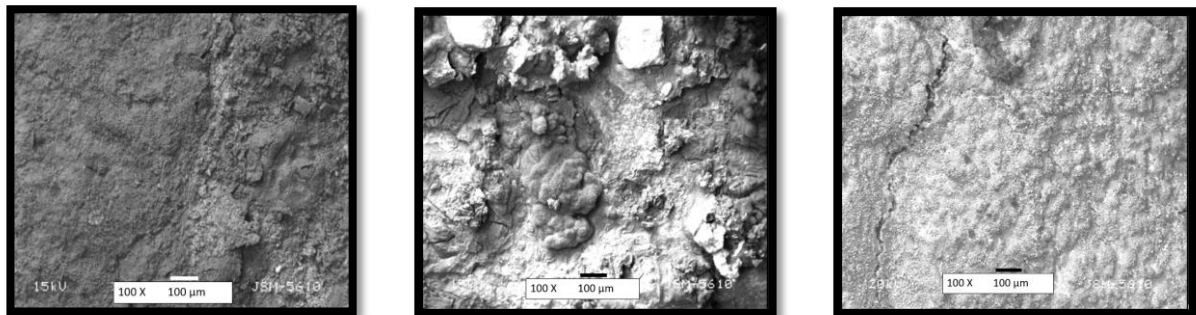


(g) Flux 7

(h) Flux 8

(I) Flux 9

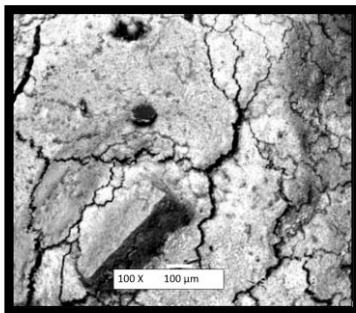
Figure 4.3 Macro Photographs of fused fluxes (10X)



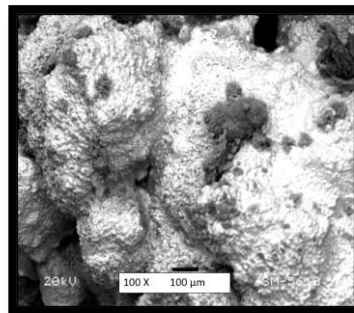
(a) Flux 1

(b) Flux 2

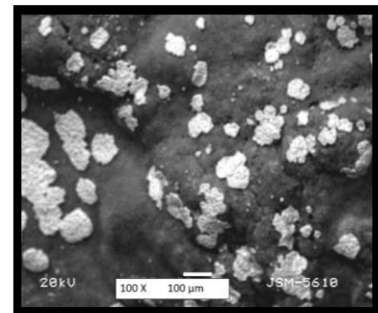
(c) Flux 3



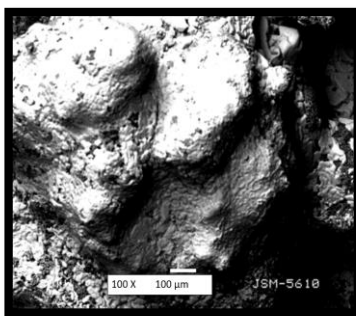
(d) Flux 4



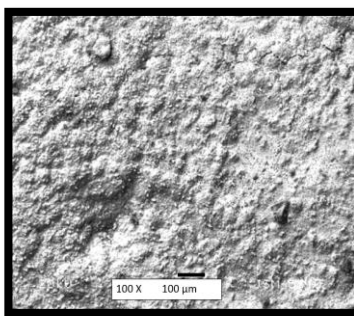
(e) Flux 5



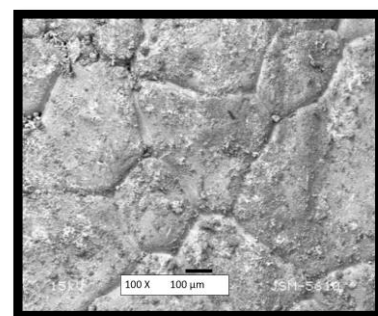
(f) Flux 6



(g) Flux 7



(h) Flux 8



(I) Flux 9

Figure 4.4 SEM analyses of all fused fluxes at 100X magnification

4.2.3 Chemical analysis of all Castings

During casting, the removal of fluxes is most important. If the flux is not removed properly from the melt surface, it forms non-metallic or intermetallic inclusions in the casting

and that affects the properties of the product. [118, 137] Inclusions in magnesium and its alloys are difficult to avoid due to the magnesium and oxygen reaction in the air to form MgO and flux reactions with oxygen to form MgO. [138] This oxide inclusion may be formed during dross and sludge operations. Above 650°C temperature, oxidation of magnesium accelerates drastically. [139] To verify the presence of magnesium and other elements, a chemical analysis of all castings is carried out using EDS analysis, as shown in Table 4.3.

Table 4.3 Composition of raw material and cast products

Material	Flux used for casting	Mg	Mn	Ca	K	Na	O
Mg Casting	Flux 1 (320)	98.51	0.16	-	-	-	1.33
	Flux 2 (220)	99.75	0.08	0.01	0.16	-	-
	Flux 3	97.91	0.03	0.01	0.05	0.02	1.98
	Flux 4 (230)	98.70	-	0.03	-	-	1.27
	Flux 5 (310)	99.87	0.04	-	0.09	-	-
	Flux 6	97.86	0.04	0.04	-	-	2.06
	Flux 7	97.82	0.08	-	0.02	-	2.08
	Flux 8	97.48	0.03	0.16	-	0.01	2.33
	Flux 9 (250)	97.89	0.32	0.04	-	-	1.75

Chemical analysis of all castings shows that a minor amount of MgO, K, Na, Ca, or Mn inclusions is present in the casting. All inclusions are present due to the use of fluxes during melting and they are found in the form of films, clusters, or oxide particles. [140, 141] Non-metallic inclusion of MgO is found in every casting except flux 2 and 5 castings. Due to the presence of a larger amount of KCl and MgCl₂ and proper handling during casting practice, magnesium oxide in flux 2 and 5 was not found. Manganese is observed in flux 1 and flux 9 due to the presence of MnCl₂ in both fluxes. Manganese is an effective element to control iron and other impurities and improve corrosion resistance so, the quality of magnesium casting is very good in the case of flux 1 and flux 9.

4.2.4 Effect of fluxes on the weight of magnesium castings

The weight loss of cast products was calculated as per equation 4.4.

$$\text{Weight loss (\%)} = \frac{(\text{Weight of pure magnesium before casting} - \text{Final weight of casting})}{\text{Weight of pure magnesium before casting}} \times 100$$

(Equation 4.4)

For fluxes 1 to 5, weight loss is quite high and it is approximately around 12 wt. % while for fluxes 6 to 9 it decreases. In the case of flux 9 weight loss is only around 6 %.

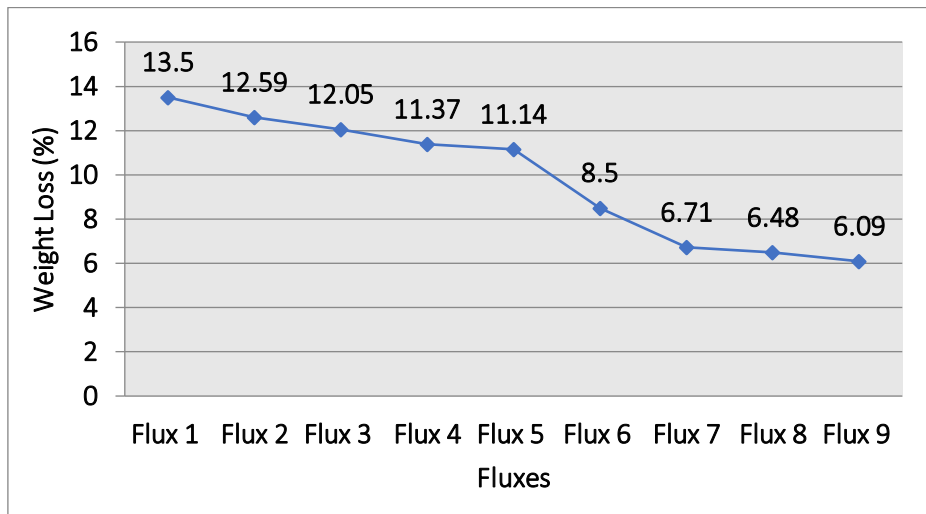


Figure 4.5 Flux v/s weight losses (%)

As per the thermal analysis result, flux 1 is decomposed at 560.7 °C but, due to the presence of magnesium oxide, a thick layer of flux was generated on the molten metal surface. It was not easily removed during casting and exposes the surface of molten magnesium to atmosphere hence oxidation is more at high temperature. So, casting developed by flux 1 has more weight loss compared to other fluxes. According to the literature, individual KCl and NaCl do not effectively break the oxide layer thus, MgCl₂ and CaCl₂ are added with them. [126] In flux 2, 3, 4, and 5, the maximum amount of KCl and MgCl₂/CaCl₂ is present and due to this around 11% to 13% weight loss occurs. Due to the proper combination of various chlorides, magnesium oxide, and/or calcium fluoride weight loss in flux 6, 7, and 8 is less which is 6.48%, 6.71%, and 8.5% respectively (Fig. 4.5). Flux 9 contains a maximum amount of MnCl₂ and KCl which control intermetallic inclusions and protect magnesium melt from oxidation. It satisfies the maximum conditions required for magnesium melting as a covering flux. The surface layer generated after using flux 9 is very thin and easily separated from solid surface hence weight loss by using flux 9 is quite less compared to all other fluxes.

4.2.5 Effect of fluxes on the mechanical properties of magnesium castings

The mechanical properties of magnesium castings can be influenced by the type of flux used during the casting process. The result of hardness, ultimate tensile strength, and ductility of all magnesium castings is shown in figure 4.6. In all magnesium castings, a negligible difference is observed in hardness and ductility value. Hardness is lying between 36 - 40 HV and ductility

value is around 8 – 10 %. The ultimate tensile strength of all castings is varying between 96 to 111 MPa. [18] Fluxes 1 to 5, which have lower levels of impurities, result in magnesium castings with higher UTS values. On the other hand, fluxes 6 to 9 contain higher levels of oxide and other impurities, which can negatively impact the UTS of the castings. The presence of these impurities can introduce defects, inclusions, or weak points within the castings, leading to a reduction in UTS. These impurities may act as stress concentrators, causing localized areas of weakness and decreasing the overall strength of the material.

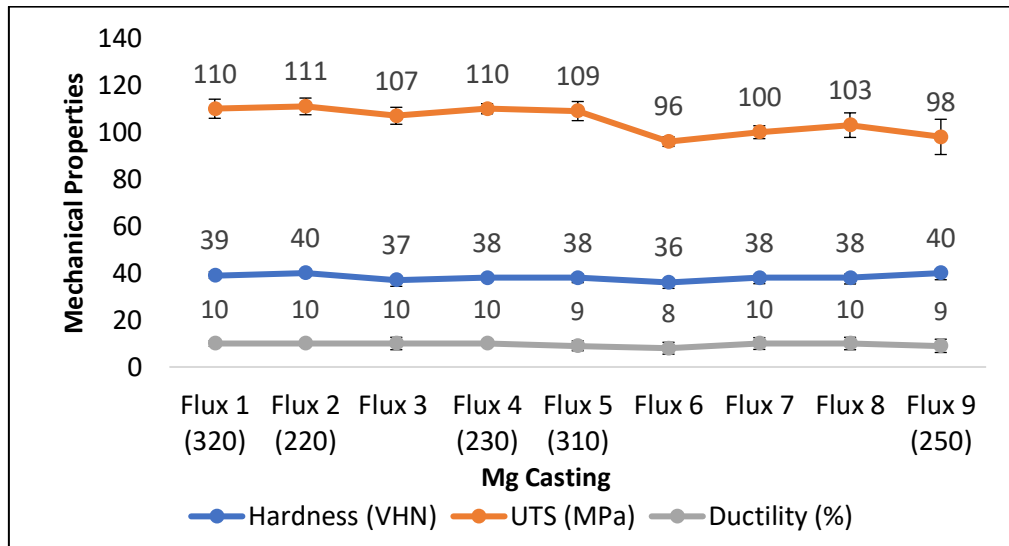


Figure 4.6 Mechanical properties of all cast products

4.3 Results & Discussion of Part II

Effect of Addition of Various Manganese Sources on Magnesium Metal

4.3.1 Chemical Analysis of Developed Systems

The chemical composition of all developed systems was determined by the Energy Dispersive Spectroscopy technique and the results for the same are shown in table 4.4.

Table 4.4 Chemical analysis of all Mg-Mn systems

System	System	Mg	Mn	O
System 1	Mg –5wt% Mn coarse powder	97.14	0.38	2.48
System 2	Mg –5wt% MnCl ₂	97.90	0.79	1.31
System 3	Mg –5wt% MnO ₂	94.35	0.85	4.80
System 4	Mg –5wt% Mn fine powder	97.11	1.05	1.84
System 5	Mg –5wt% Mn electrolytic flakes	95.89	2.66	1.45

4.3.2 Surface Morphology of All Manganese Forms

The shape and size of all manganese forms were studied in a scanning electron microscope. This analysis was done at 35 X, 50 X or 100 X magnifications to properly analyze the size and shape of manganese particles. Surface images of all manganese forms are shown in figure 4.7.

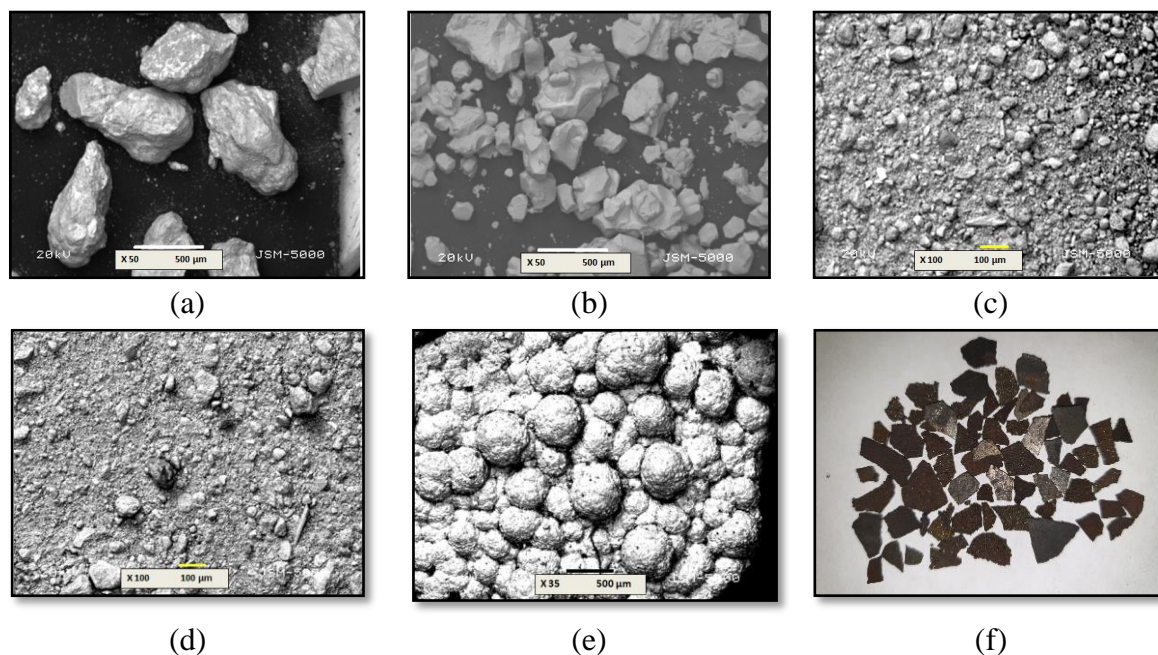


Figure 4.7 SEM images of manganese forms (a) Manganese coarse powder (b) MnCl_2 powder (c) MnO_2 powder (d) Manganese fine powder (e) Electrolytic Manganese flakes and (f) camera image of electrolytic Manganese flakes

As shown in figure 4.7 (a), manganese coarse powder is anti-adhesive and irregular in shape. The average diameter of these particles is around 0.593 mm. In the case of MnCl_2 , the powder looks sticky due to the presence of Cl as a moisture absorbent nature. This powder particles are small in size, rounded with sticky nature which is shown in figure 4.7 (b). The size of MnCl_2 powder is around 0.193 mm. As per figure 4.7 (c) & (d) shape, the size and distribution of MnO_2 powder and manganese fine powder are nearly the same. Both are rounded and sticky. The size of MnO_2 powder and manganese fine powder is 0.065 mm and 0.0610 mm respectively. The size of electrolytic manganese flakes is around 4.497 mm which is higher than other manganese forms. Figure 4.7 (e) shows the surface of one manganese particle. The SEM image of Electrolytic manganese flakes looks like a spherical shape with bubbles on its surface due to high magnification. Figure 4.7 (f) shows the actual size (thickness, length) and shape of Electrolytic manganese flakes at 10X magnification.

4.3.3 Manganese Recovery in Magnesium at 850°C

As discussed in section 2.4, researchers have a different opinion about the solubility of manganese in magnesium. The greater part of the accessible data is on the Mg-rich side describing the limited solid solubility of manganese in magnesium. So, in this part II, different forms of manganese sources were used and study their recovery in magnesium. Figure 4.8 shows manganese recovery in magnesium from different sources at 850°C. Manganese recovery from manganese coarse powder is very less, which is 0.38 wt.%. When manganese was added as MnCl₂, it will react with magnesium and form MgCl₂ and Mn (Equation 4.5). [62]



This MgCl₂ is helpful to create a surface layer on a molten metal surface and protect it from the burning. In this system, high HCl emission was occurring due to the reaction of the chlorides with moisture from the air, and the efficiency of recovery is also less. Only, 0.79 wt.% manganese present in this system. Manganese recoveries from MnO₂ and manganese fine powder containing systems are 0.85 wt.% and 1.05 wt.% respectively which higher than MnCl₂. In the case of MnO₂ and fine powder recovery of manganese is more because of the higher content of Mn. As shown in equation 4.6, Manganese from MnO₂ sources reacts with magnesium and forms some magnesium oxide.



The maximum recovery of manganese is achieved from electrolytic pure manganese flake which is 2.66 wt.% at 850°C which is highest than other sources of manganese. It may be due to its proper size, shape, and purity than other sources of manganese. % Solubility depends on types of manganese grade, size, and temperature. Here, temperature and holding time are fixed say 850°C and 1 hour respectively for all systems but solid manganese sources are differing by its size, shape, and chemical nature. The purity of the manganese source also plays a major role in recovery, which is best in the case of electrolytic grade flake shape samples.

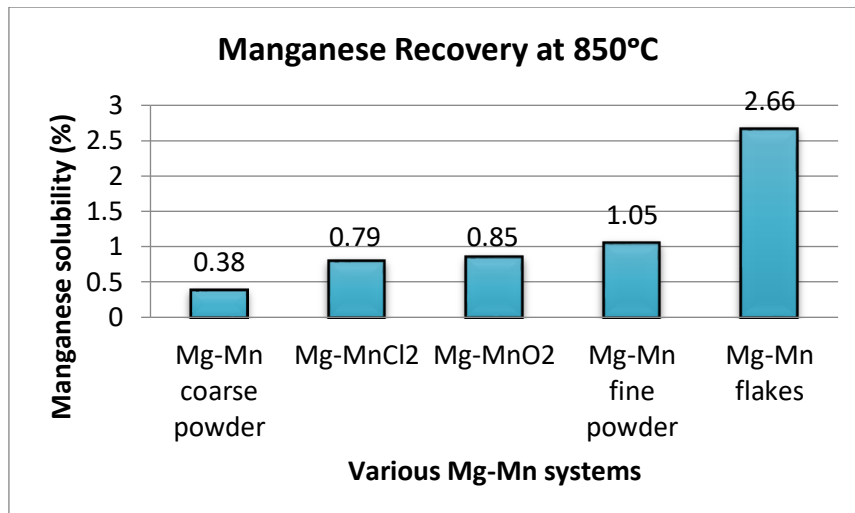
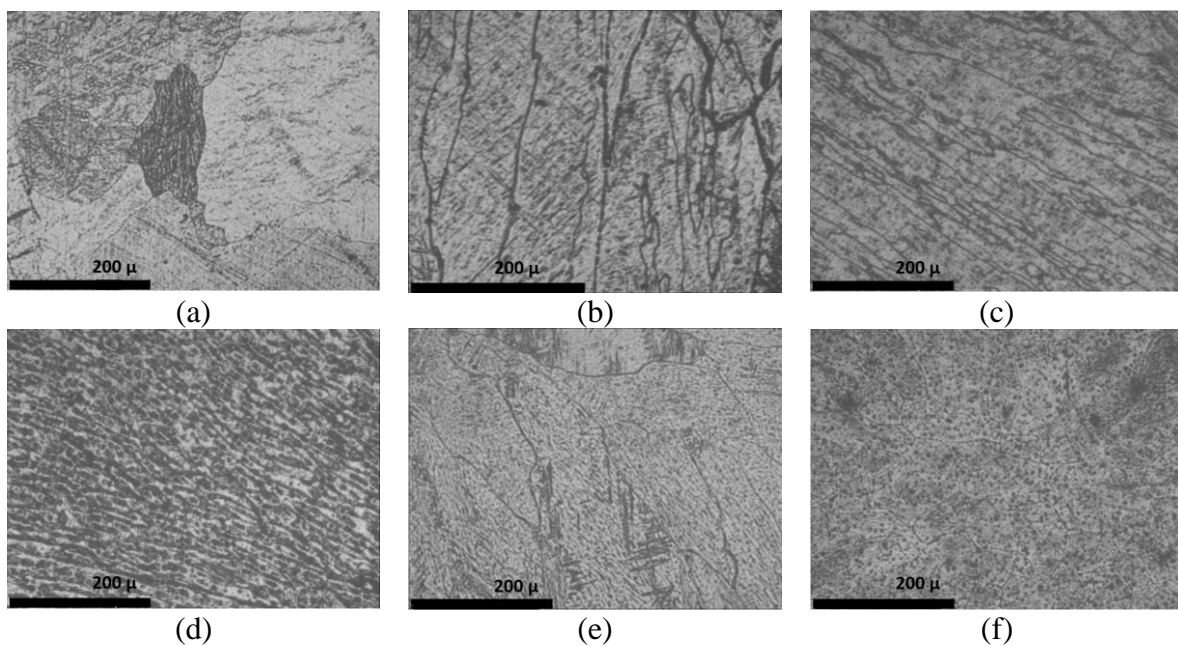
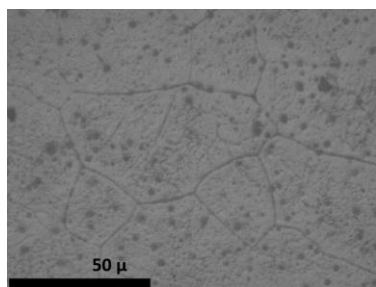


Figure 4.8 Recovery of Manganese from its different sources at 850°C in Pure Mg metal

4.3.4 Microstructure Analysis of All Systems

After solidification in grey cast iron metallic die, samples were analyzed to get a better understanding of their behaviour in terms of microstructure and mechanical properties. As shown in figure 4.9 (a), non-uniform, large coarse grain structure was observed in pure magnesium casting. As per literature, if molten magnesium heated further in the range of 150°C to 300°C more than its liquids temperature than cast products grain is refined. [142] So, for better grain refinement and to increase manganese solubility, in all Mg-Mn systems, molten magnesium melt was superheated at 850°C.





(g)

Figure 4.9: Optical Micrograph of magnesium & all systems (a) Pure Mg (b) Mg- Mn coarse powder system (c) Mg-MnCl₂ powder system (d) Mg-MnO₂ powder system (e) Mg-Mn fine powder system (f) Mg-Mn flakes system at 100 X and (g) Mg-Mn flakes system at 400X

Pure magnesium structure was changed from a coarse-grained to a fine-grained due to the presence of manganese and superheating. Original pure magnesium sample has always a big size grain structure but as the amount of manganese changes, structure refines, and bands were observed. In the case of MnO₂ powder, shapes of bands become lamellar just like pearlite in steel structure (Fig. 4.9 d) and very fine in case of fine powder manganese source (Fig. 4.9 e). As the recovery of manganese increases, very fine phases of Mg-Mn or Fe-Mn or combination of Mg-Mn-Fe are seen. Overall, microstructures exhibited relatively a fine structure as manganese content increases. [73] As shown in figure 4.9, less manganese-containing systems were coarse and non-uniform structure. In the case of the highest recovery of manganese (electrolytic Mn flakes), a more uniform and refined grain structure was observed due to the presence of 2.66 wt.% manganese which is shown in figure 2 (f) & (g). Spherical dot shape manganese inter-metallic particles are also observed in the Mg-Mn flakes system. This precipitate looks dark in color and present inside the grains and at the grain boundaries as shown in figure 2(g).

As per literature, when the difference in atomic radii between the two atom types is less than about 15% then the substitutional solid solution will form. Otherwise, the solute atoms will create a new phase. [18,19] In the case of the Mg-Mn system, the atomic radius of magnesium and manganese are 0.160 nm and 0.112 nm respectively. [145] Atomic size difference of magnesium and manganese is around 30% so, the chances of the substitutional solid solution are very less and it makes precipitates depending upon other impurities.

Previous research indicates that the Mn-enriched particles observed in the Mg-Mn alloy are exclusively attributed to the precipitation of the Mn phase, which serves as the sole precipitate phase in the Mg-rich region of Mg-Mn binary alloys. [69] The XRD analysis shown

in figure 4.10 confirms the presence of Mn and pure magnesium phases in the Mg-Mn flakes system. Due to less amount of manganese present in Mg-MnCl₂ and Mg-MnO₂ powder system, only magnesium phase is detected in their XRD results.

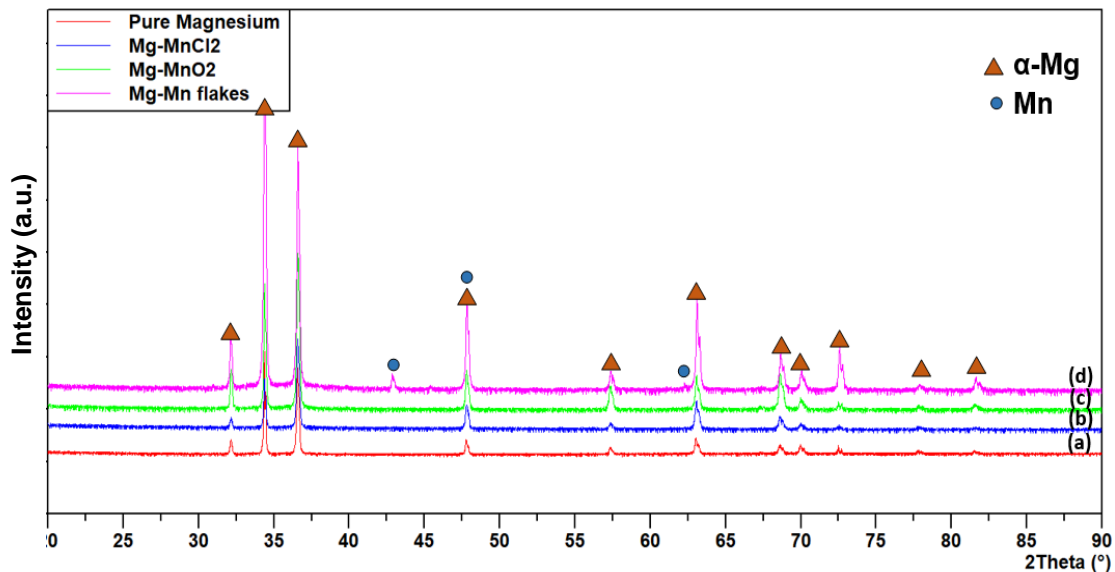


Figure 4.10 XRD pattern of (a) Pure magnesium (b) Mg-MnCl₂ powder system (c) Mg-MnO₂ powder system (d) Mg-Mn flakes system

4.3.5 Mechanical Properties

Figure 4.11 shows hardness, ultimate tensile strength, and % elongation of all developed Mg-Mn systems. As shown in figure 4.11, by addition of manganese hardness and ultimate tensile strength of magnesium is increased. The hardness value of Mg-Mn systems is more compare to pure magnesium. It increases from 38HV to 58HV due to the solid solutionizing effect. For all manganese-containing systems, the negligible difference is observed in hardness value which is 55 HV to 58 HV. The negligible difference in hardness values can be attributed to several factors. At lower manganese concentrations, the solid solution strengthening effect on magnesium is relatively small, resulting in minimal variation in hardness. However, in systems with higher manganese content, the formation of Mn precipitates is more that can contribute to increased hardness. It acts as strengthening phases within the material.

Up to 1% manganese, the ultimate tensile strength value is nearly the same. Due to the presence of magnesium oxide, the ultimate tensile strength value of the MnO₂ containing system is less. Maximum UTS is achieved in electrolytic manganese flakes containing system 5 i.e. 140 MPa. There is negligible change in % elongation is observed up to 1% manganese.

In system 5, because of more amounts of manganese and higher strength, % elongation is nearly 50% less compared to other systems. Chlorine helps to protect the surface layer of molten metal and control the changes of the oxidation potential of magnesium metal at high temperature so, the chances of oxide formation are less. Due to this, the highest elongation is obtained in the case of the Mg-MnCl₂ system, which is better and around 25% higher than pure magnesium metal. All improvement in mechanical properties is due to the presence of manganese only and this data are not available anywhere in literature for comparison purposes.

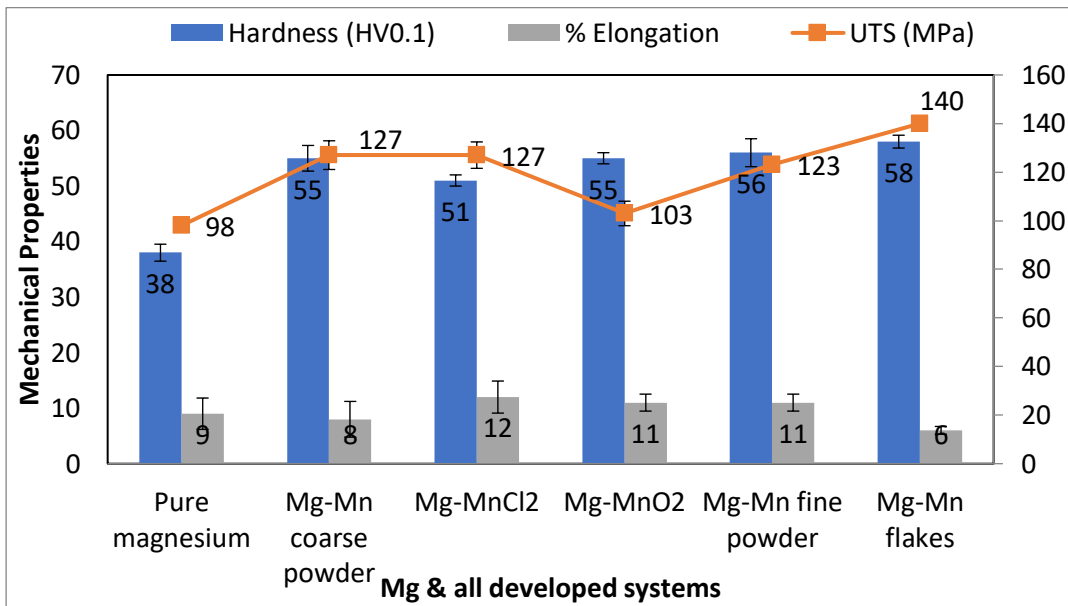


Figure 4.11 Hardness and tensile properties of all Mg-Mn systems

4.3.6 Corrosion Behaviour

As discussed in section 3.11, corrosion rate of the all-developed systems measured by weight loss method in mpy. Density results used for calculations of corrosion rate of all systems are shown in figure 4.12.

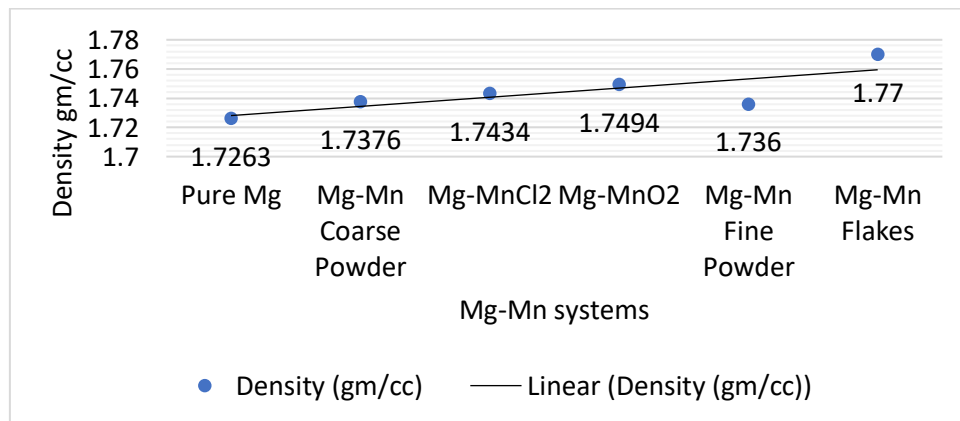


Figure 4.12 Density of all Mg-Mn systems

In a study conducted by Makar and Kruger, [95] it was found that films formed on magnesium surfaces immersed in 3% sodium chloride solution consist of various compounds such as $Mg(OH)_2$, $MgCl_2 \cdot 6H_2O$, $Mg_3(OH)5Cl \cdot 4H_2O$, and MgH_2 . These compounds were identified through infrared spectroscopy and X-ray diffraction analysis. As shown in figure 4.3, the corrosion rate of pure magnesium after 24 hours of immersion was relatively high (91.33 mpy), but it decreased to 30.86 mpy after 48 hours. This can be attributed to the formation of a protective layer $Mg(OH)_2$, on the surface of magnesium. When magnesium comes into contact with water in the presence of NaCl, $Mg(OH)_2$ is formed, acting as a barrier that slows down the corrosion process. Initially, the protective film may not fully develop within the first 24 hours, resulting in a higher corrosion rate. However, with prolonged exposure time (48 hours), the $Mg(OH)_2$ film has more opportunity to grow and provide enhanced protection, leading to a decrease in the corrosion rate.

As per research, when sample was immersed in chloride solution, colour of its surface becomes darker due to the cathodic activation (shown in figure 4.14). These corroded areas are cathodically active, which promotes hydrogen evolution. [146] As reviewed by Liming Xu et.al. the cathodic activation caused by metallic Mn is moderately strong because it has a standard electrode potential near to that of magnesium. As a result, hydrogen evolution reactions (HER) are prevented by the development of a dense Mn-rich corrosion layer. [147, 148] Here, in Mg-Mn flakes system, maximum amount of manganese (2.66 wt.%) is present which creates Mn-rich passive layer on sample surface and decrease the corrosion rate. Maximum corrosion rate was observed in Mg-Mn coarse powder system. As show in figure 4.14, large size pits are observed in this system. It may be possible due to the presence of casting defects in this system.

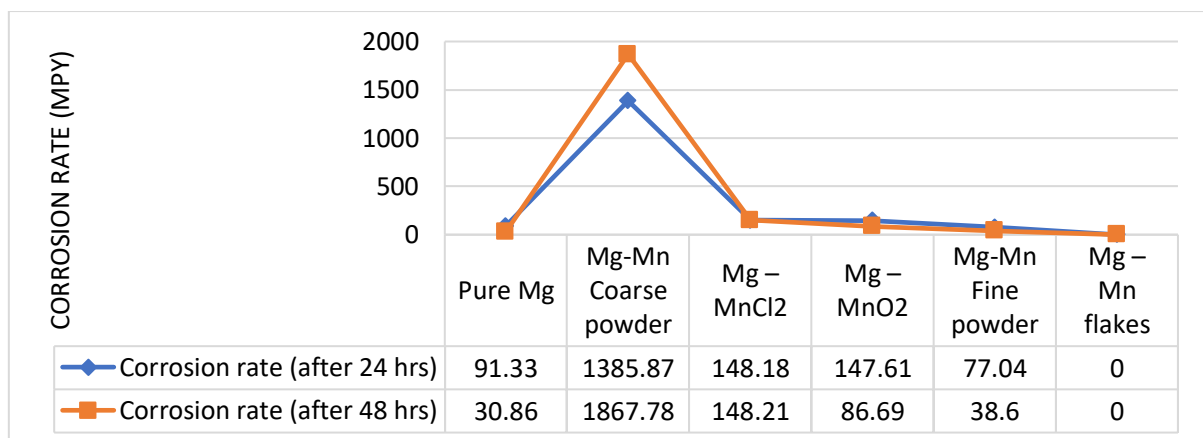


Figure 4.13 Corrosion rate of all Mg-Mn systems

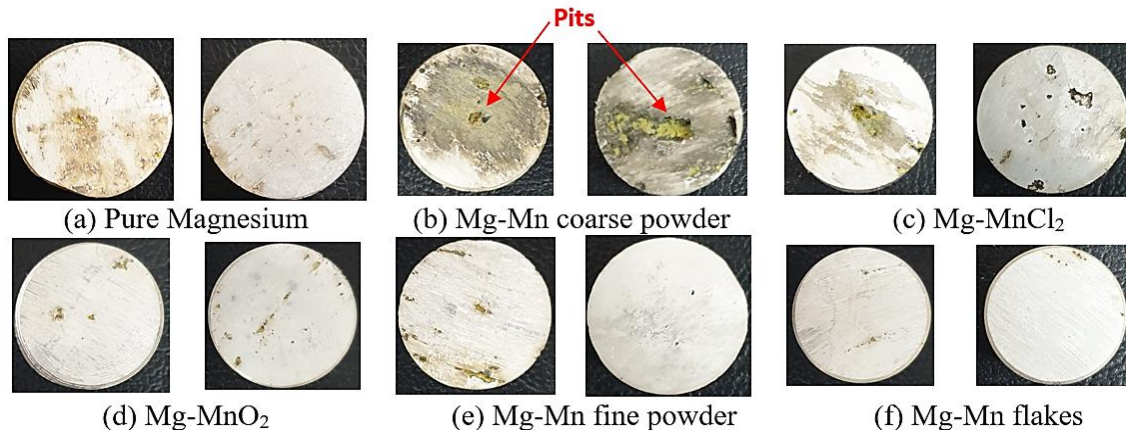


Figure 4.14 Photographs of the (a) Pure magnesium (b) Mg-Mn coarse powder system (c) Mg-MnCl₂ system (d) Mg-MnO₂ system (e) Mg-Mn fine powder system (f) Mg-Mn flakes system after 24 hrs and 48 hrs immersion in 3.5 wt. % NaCl

4.4 Results & Discussion of Part III

Effect of Temperature on Solubility of Manganese in Magnesium

4.4.1 Chemical Analysis of Developed Systems

Maximum recovery was obtained in case of Mg-Mn flakes. Thus, Mg-5wt% Mn flakes system was selected to understand the role of various temperature on the recovery of manganese in magnesium. The chemical composition of Mg-Mn flakes systems at different temperatures is shown in table 4.5.

Table 4.5 Chemical analysis of all Mg-Mn systems at different temperature

System	System	Temperature	Mg	Mn	O
System 6	Mg -5wt% Mn flakes	750 °C	91.43	0.3	8.27
System 7	Mg -5wt% Mn flakes	800 °C	92.57	1.7	5.73
System 8	Mg -5wt% Mn flakes	850 °C	95.89	2.66	1.45
System 9	Mg -5wt% Mn flakes	900 °C	90.38	3.01	6.61
System 10	Mg -5wt% flakes	950 °C	90.03	3.46	6.50

4.4.2 Manganese Recovery in Magnesium at Different Temperatures

Figure 4.15 shows manganese recovery in magnesium at different temperatures. As per the Mg-Mn binary diagram (discussed in section 2.4), at 653°C magnesium precipitates out of L + α -Mn in a peritectic reaction. Solubility of manganese in magnesium is depend on the temperature. If temperature decrease, solubility of manganese also decreases and due to that

more amount of Mn precipitates. [70] Here, as shown in figure 4.15, manganese recovery is increasing by increasing temperature. The maximum manganese amount is found at 950°C temperature.

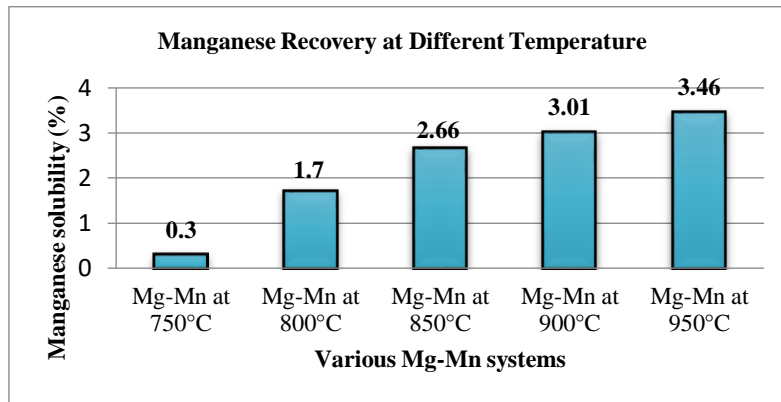


Figure 4.15 Recovery of manganese in pure magnesium at different temperature

4.4.3 Microstructure Analysis of All Systems

In the microstructure analysis of all systems, as discussed in part II, the presence of manganese in Mg-Mn alloys has been found to refine the grain structure of pure magnesium. This is evident in figure 4.16 a, b, c, where the grains of magnesium alloys containing manganese are observed to be finer compared to pure magnesium. However, it is important to note that higher superheating temperatures have shown adverse effects on the grain structure. At elevated temperatures, the solubility of manganese increases, resulting in larger grain sizes. This is particularly observed in Mg-Mn alloys with manganese content exceeding 3%.

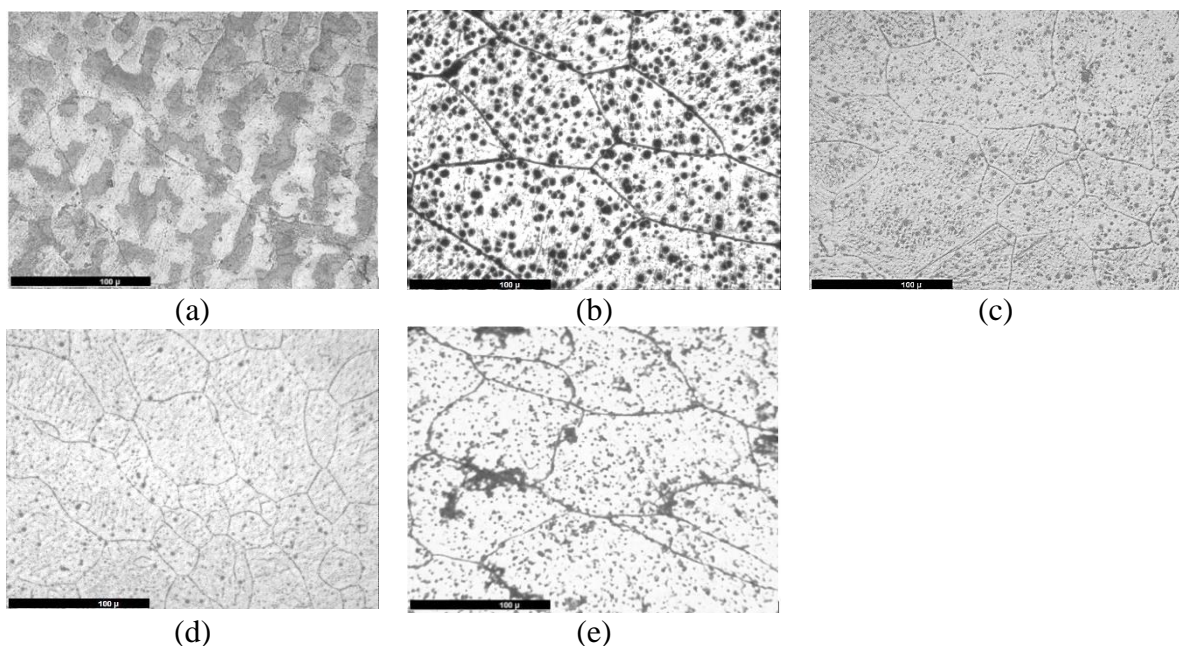


Figure 4.16 Optical Micrograph of all Mg-Mn systems at (a) 750 °C (b) 800 °C (c) 850 °C (d) 900 °C (e) 950 °C (at 200 X)

Figures 4.16 d and e demonstrate that alloys with higher manganese concentrations exhibit larger grain sizes. The grain sizes of the Mg-Mn alloys vary with different manganese content and superheating temperatures. System 6 exhibits a grain size of 123.9 microns, while system 7 has a slightly smaller grain size of 111.8 microns. The grain sizes further decrease to 47.11 microns for system 8 and 50.27 microns for system 9. System 10 shows a grain size of 108.7 microns.

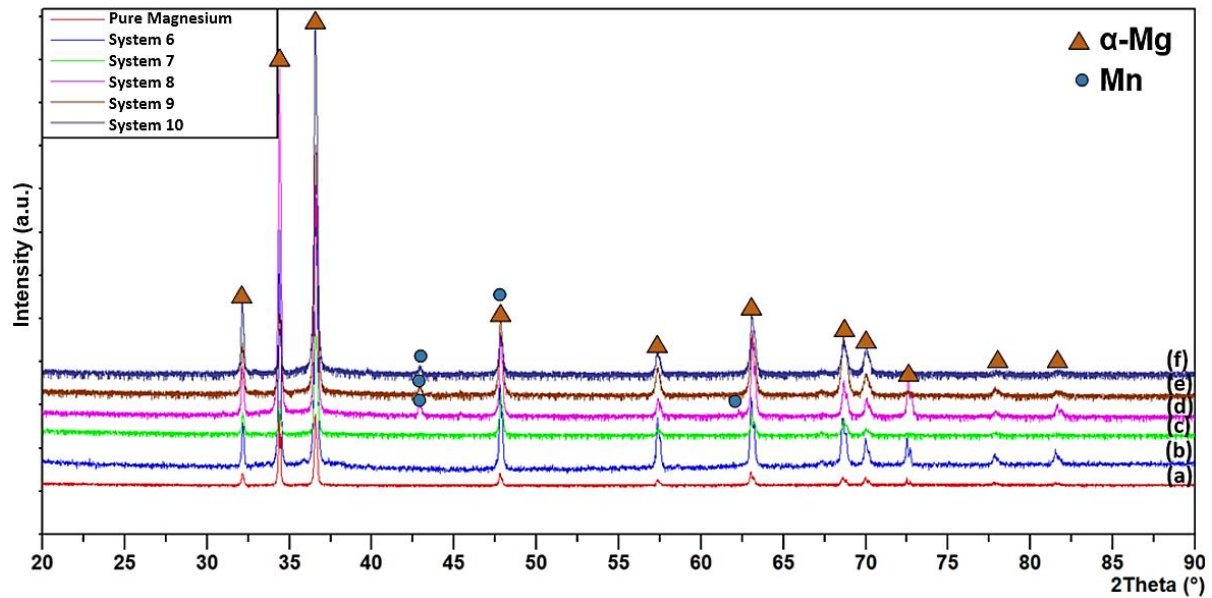


Figure 4.17 XRD Pattern of (a) Pure magnesium (b) Mg-Mn flakes at 750°C (c) Mg-Mn flakes at 800°C (d) Mg-Mn flakes at 850°C (e) Mg-Mn flakes at 900°C (f) Mg-Mn flakes alloy at 950°C

According to the temperature-solubility nucleation theory, at specific temperatures, stable compounds can form in molten alloy. This idea is based on the procedure in which the molten alloy is once superheated to a specific temperature, quickly cooled to the casting temperature, and then poured into the mould. [65] As per the XRD results, in Mg-Mn systems, pure Mg and Mn phases are present (Fig. 4.17).

4.4.4 Mechanical Properties

Figure 4.18 shows the hardness, ultimate tensile strength, and % elongation of all developed Mg-Mn systems. The presence of manganese increases the hardness and ultimate tensile strength of pure magnesium and decreases the % elongation. Maximum UTS and hardness are observed in Mg-2.66%Mn alloy (at 850°C) i.e. 140 MPa and 58 HV0.1 respectively.

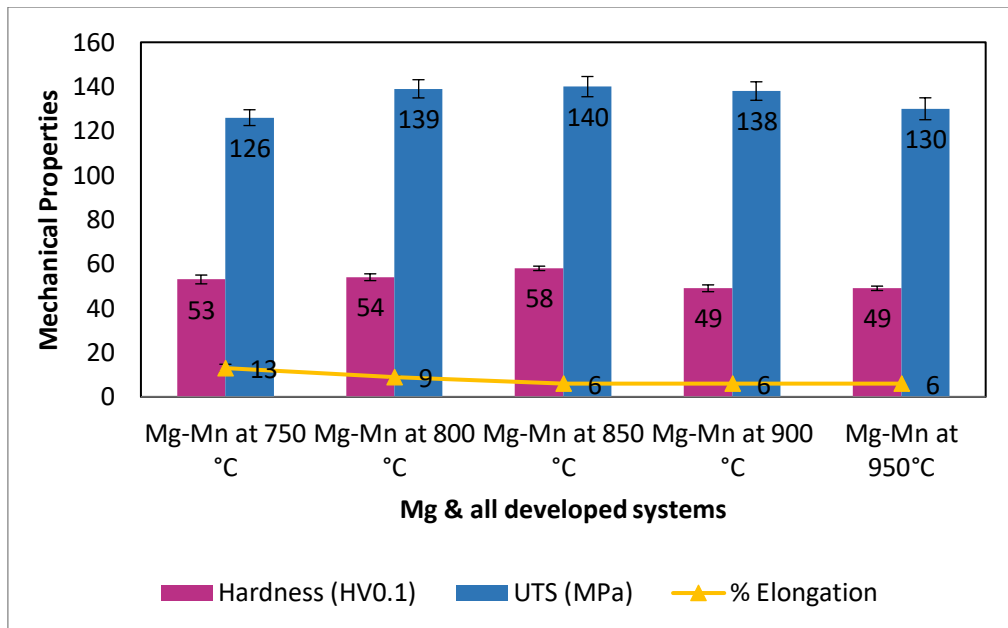


Figure 4.18 Hardness and tensile properties of all systems

4.4.5 Corrosion Study

The size, distribution, type, and composition of the intermetallic particles that precipitate during cooling from the casting temperature are some of the variables that affect corrosion rate. By regulating these variables, alloys with enhanced corrosion characteristics can be created. [34] As discussed in section 2.4, presence of manganese in magnesium alloy increases the corrosion resistance. As a results, In Mg-Mn flakes containing systems show excellent corrosion resistance. Mg-Mn systems containing 1.7 wt. % Mn, 2.66 wt.% Mn, 3.01 wt.% Mn, 3.46 wt.% Mn shows outstanding corrosion resistance (0 mpy after 24 hrs and average 12 mpy after 48 hrs). In the entire surface of these alloys, shows uniform corrosive layer. Hydroxide layer is observed in magnesium surface. However, Mn and Mg don't form any compounds, Mn particles are essentially in elemental form. So, around the manganese particle, hydroxide film of Mg is absent. [149] In Mg-0.3Mn (750°C) system, high corrosion rate found i.e. 371 mpy and 308 mpy for 24 hrs and 48 hrs respectively. Surface of the all Mg-Mn systems after 24 hrs and 48 hrs.

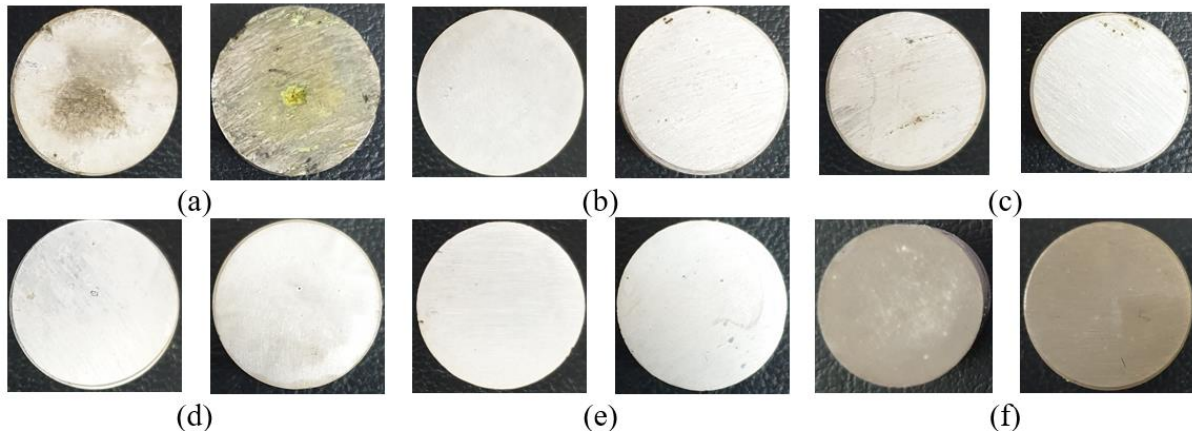


Figure 4.19 Photographs of the (a) Mg-Mn flakes at 750°C (b) Mg-Mn flakes at 800°C (c) Mg-Mn flakes at 850°C (d) Mg-Mn flakes at 900°C (e) Mg-Mn flakes at 950°C system after 24 hrs and 48 hrs immersion in 3.5 wt. % NaCl after cleaning (f) Mg-Mn flakes at 950°C system before cleaning

4.5 Results & Discussion of Part IV

Develop and Study the Mg-Cu and Mg-Cu-Mn (CM) Alloys

4.5.1 Chemical Analysis of Developed Systems

The chemical composition of all developed system is shown in table 4.6.

Table 4.6 Chemical analysis of Mg-Cu-Mn alloys

System	Alloy	Cu	Mn	O	Mg
System 11	Mg-1Cu (CM10)	0.91	0.45	2.92	Balance
System 12	Mg-2Cu (CM20)	1.87	0.61	4.73	Balance
System 13	Mg-3Cu (CM30)	2.57	0.47	3.33	Balance
System 14	Mg-1Cu-1Mn (CM11)	0.76	1.12	3.58	Balance
System 15	Mg-2Cu-2Mn (CM22)	1.83	2.54	5.13	Balance
System 16	Mg-3Cu-2Mn (CM32)	2.79	2.32	4.47	Balance

4.5.2 Microstructure Analysis of All Systems by Optical Microscopy and SEM analysis

Figure 4.20 shows the optical microstructures of the Mg-Cu and Mg-Cu-Mn alloys. The microstructure is composed of α – base magnesium, eutectic phase, and some isolated particles dispersed inside the grains. The eutectic phase is distributed along the grain boundaries. As

seen in figure 4.20 (a, b, c), with increasing copper content size of eutectic phases is progressively changed. Furthermore, the grain size is observed to become finer as the copper content increases. According to Yu Zhang and J. Buha, the addition of copper can refine the microstructure by reducing the solidification time. [96, 150] The measured grain sizes for the CM10, CM20, CM30, CM11, CM22, and CM32 alloys are 79.30 μ , 38.47 μ , 25.12 μ , 41.83 μ , 29.01 μ , and 32.14 μ , respectively. It is evident that the microstructures of manganese-containing Mg-Cu alloys exhibit greater refinement compared to alloys containing only copper. However, in the case of the CM32 alloy, which contains both copper and manganese, the grain size is slightly larger than that of the CM30 alloy. The presence of manganese in combination with copper may have influenced the grain growth, resulting in a slightly increased grain size compared to the alloy containing only copper.

As shown in figure 4.20 (d), when 1.12% manganese is present (CM11 alloy), the microstructure is refined up to some extent. It is found that the CM22 alloy microstructure contains α -Mg, eutectic phases, and a high amount of isolated particles inside the grains (Fig. 4.20 (e)). In CM32 alloy, as mention in figure 4.20 (f), mixture of Mg-Cu-Mn indicate the continuous network form of Mg_2Cu . The same phenomena is very easily observed in case of SEM photographs. A heterogeneous nucleation effect of Mn-containing particles during solidification may be a major contributing factor to grain refinement. [151, 152]

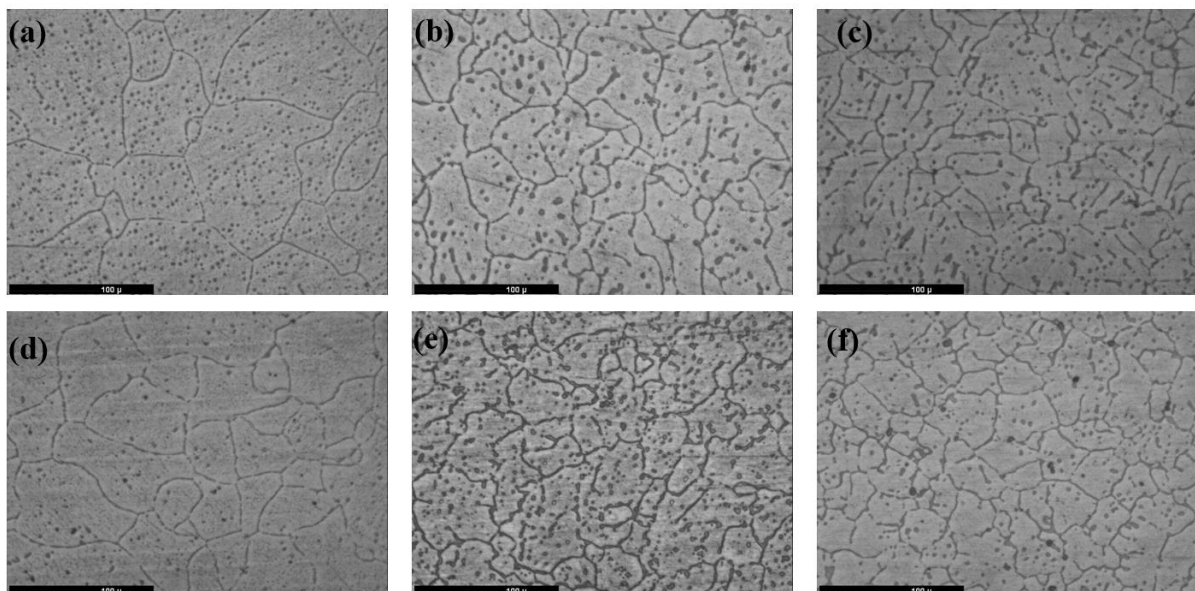


Figure 4.20 Optical Micrographs of the as cast alloys at 200 X (a) CM10 (b) CM20 (c) CM30 (d) CM11 (e) CM22 (f) CM32

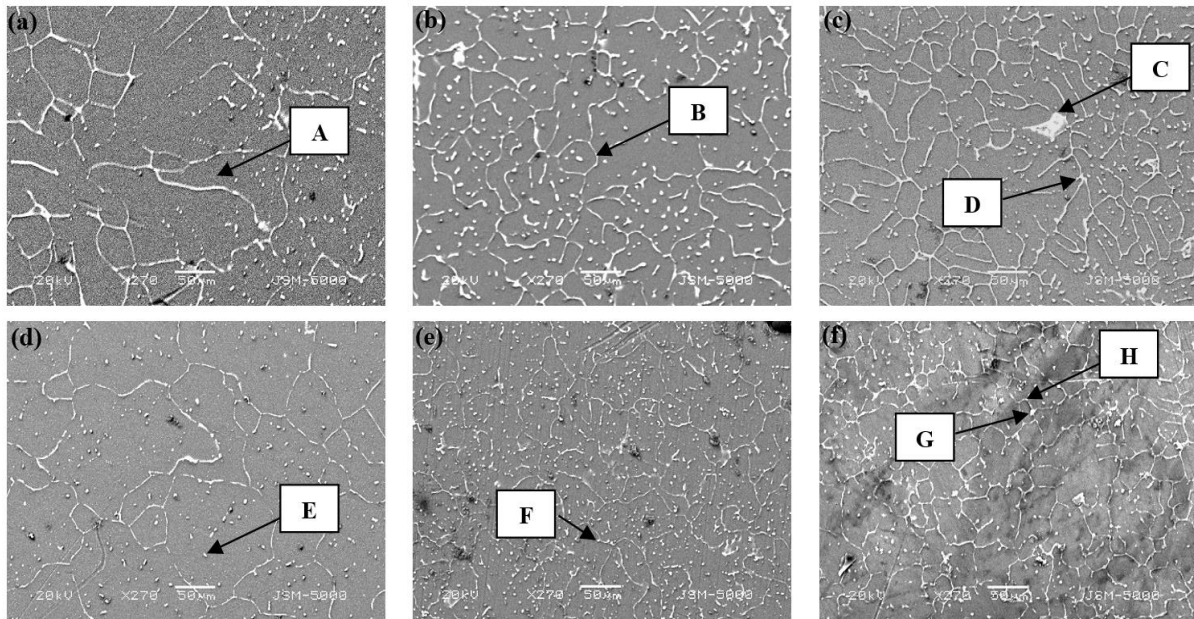


Figure 4.21 SEM Micrographs of the as cast alloys at 270 X (a) CM10 (b) CM20 (c) CM30 (d) CM11 (e) CM22 (f) CM32

SEM micrographs (270 X) with corresponding EDS analysis of the alloys are given in figure 4.21 and Table 4.7, respectively. As shown in figure 4.21, the eutectic morphology of the Mg-Cu is affected by manganese content. Based on EDS analysis at a particular area, the grey area (marked A) is observed as an α -Magnesium phase. The bright precipitate at the grain boundaries (marked B) of the alloy is rich in Cu. The eutectic morphology is changed in 3 wt. % Cu-containing alloy. (Marked as C & D). Based on the EDS analysis, XRD analysis, and available literature phase identified as Mg_2Cu . [96, 103] The developed intermetallic of Mg-Cu-Mn observed in CM11, CM22, and CM32 alloy which is presented in figure 4.21 (d, e, f). The isolated bright particle is inferred as the Mn-Mg phase according to EDS. (Marked G)

Table 4.7 Chemical compositions of as-cast Mg-Cu and Mg-Cu-Mn alloys (weight %)

Location (point)	Mg	Cu	Mn	O	Other
Figure 17 (a), A	100	-	-	-	-
Figure 17 (b), B	77.89	8.32	0.39	13.00	0.40
Figure 17 (c), C	79.62	18.43	-	1.95	-
Figure 17 (c), D	64.50	21.18	-	13.56	0.76
Figure 17 (d), E	74.07	16.01	0.25	9.41	0.25
Figure 17 (e), F	18.33	0.43	75.28	3.91	2.04
Figure 17 (f), G	4.24	-	91.14	3.40	1.21
Figure 17 (f), H	70.18	22.87	1.09	5.86	-

The XRD results of pure magnesium and all Mg-Cu and Mg-Cu-Mn alloys are shown in figure 3. The Mg-Cu alloy consists of α -Mg and Mg_2Cu phases whereas Mg-Cu-Mn alloys consist of α -Mg, Mg_2Cu , and α -Mn phases. The α -Mg, Mg_2Cu , and α -Mn phases have a hexagonal, face-centered orthorhombic, and primitive cubic structure respectively. The intensity and number of Mg_2Cu peaks increases with the increasing Cu content.

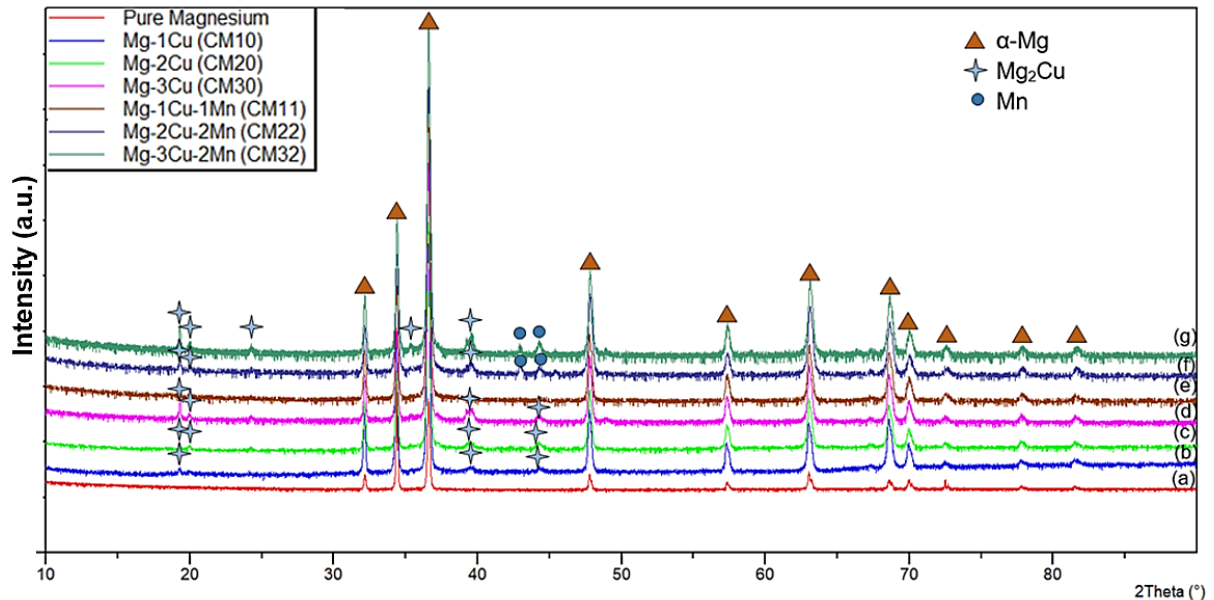


Figure 4.22 XRD patterns of (a) pure magnesium (b) CM10 (c) CM20 (d) CM30 (e) CM11 (f) CM22 (g) CM32 alloys

4.5.3 Mechanical Properties

Figure 4.23 shows the ultimate tensile strength, Vicker's hardness (HV0.1), and % elongation of as-cast Mg-Cu and Mg-Cu-Mn alloys. Mechanical properties of the alloys have a significant relation to the presence of eutectic, intermetallic, and its amount and distribution. [153] The morphology of intermetallic is changing by increasing the amount of Cu and Mn (Fig. 1). As shown in figure 4.23, the ultimate tensile strength of Mg-1Cu (157 MPa) is higher than Mg-2Cu (152 MPa) and Mg-3Cu (149 MPa). Increasing the Cu amount does not lead to an increase in UTS value, it is almost in the same range. [96] However, due to the presence of the Mg_2Cu phase, the ultimate tensile strength of all Mg-Cu alloys is high compared to pure magnesium. [153, 154] 2 % Manganese containing Mg-Cu alloys have more ultimate tensile strength compared to only Mg-Cu alloys. Vicker's hardness of Mg-Cu and Mg-Cu-Mn alloys are lying between 20 to 55 HV. Maximum hardness is achieved in CM32 alloy i.e. 55 HV. % Elongation of 1 wt. % Cu-containing alloy is 11 % which is the highest among the other alloys. By the addition of more amount of Cu and Mn % elongation is decreased.

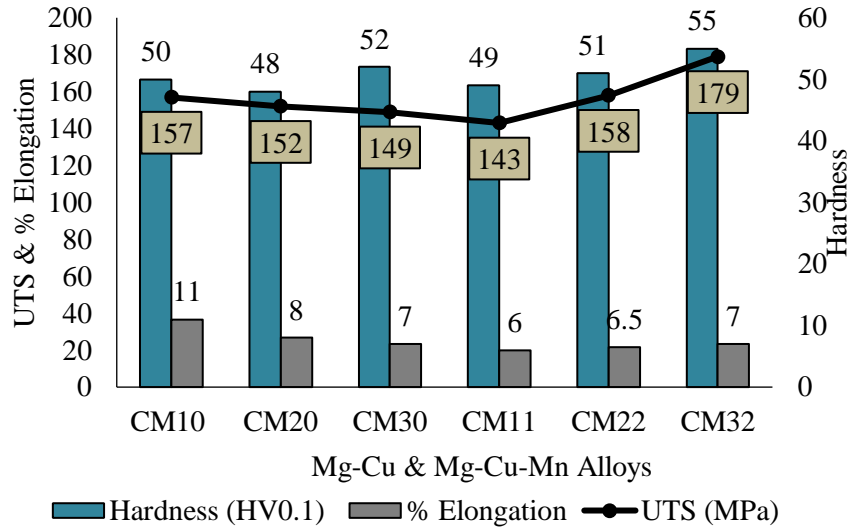


Figure 4.23 Room temperature mechanical properties of as cast Mg-xCu and Mg-xCu-yMn alloys ($x = 1, 2, 3$) and ($y = 1, 2$)

4.5.4 Corrosion Behaviour

The density of all alloys is shown in figure 4.24. The results show that the density of the alloys varies slightly, with values ranging from 1.74 g/cm³ for the CM10 alloy to 1.81 g/cm³ for the CM22 alloy. These differences in density may be due to variations in the composition of the alloys, as well as variations in the measurement process.

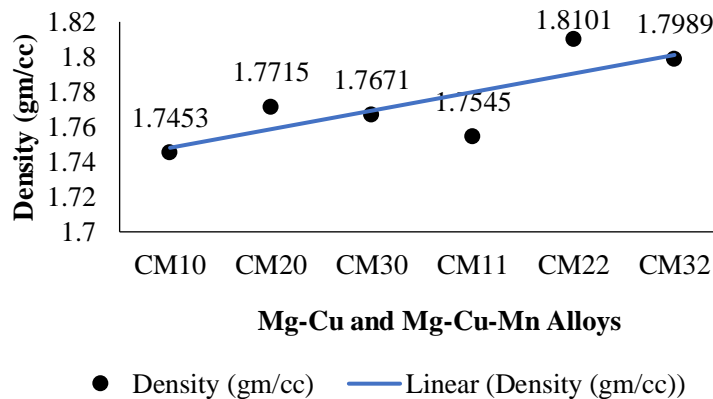


Figure 4.24 Density of all Mg-Cu and Mg-Cu-Mn alloys

The addition of manganese to the alloys has been observed to have a positive impact on corrosion mitigation, as demonstrated by the lower corrosion rate observed in the CM11 alloy compared to the CM10 alloys. The images of the alloys (Fig. 4.25 a & b and Fig. 4.26) after immersion in the 3.5 wt.% NaCl solution reveal an increasing severity of corrosion with higher copper content, with the CM30 alloy exhibiting the most severe corrosion.

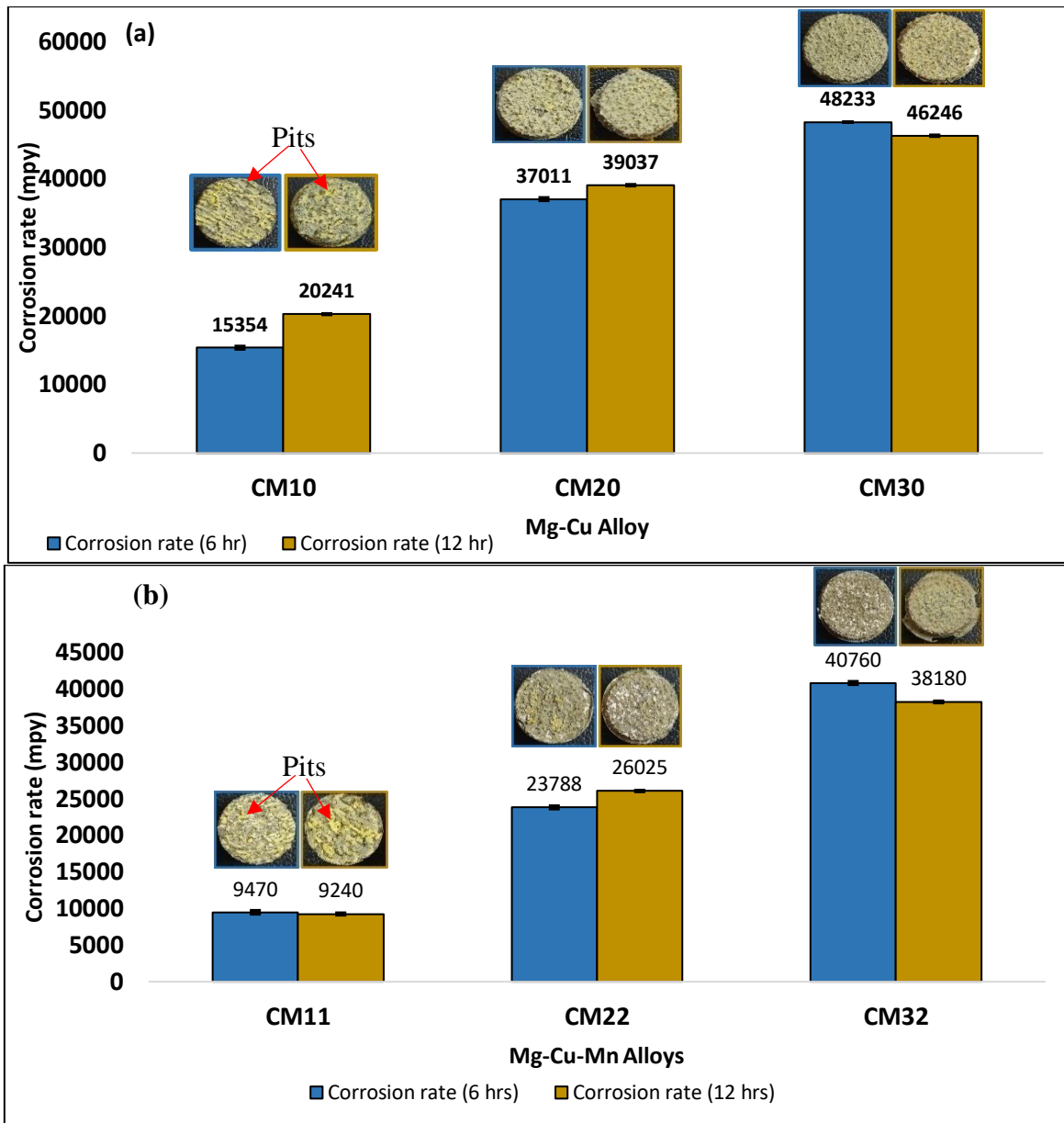


Figure 4.25 Corrosion rates (mpy) after 6 hrs and 12 hrs immersion in 3.5 wt. % NaCl (a) Mg-xCu alloys (b) Mg-xCu-yMn alloys (x = 1, 2, 3) and (y = 1, 2)

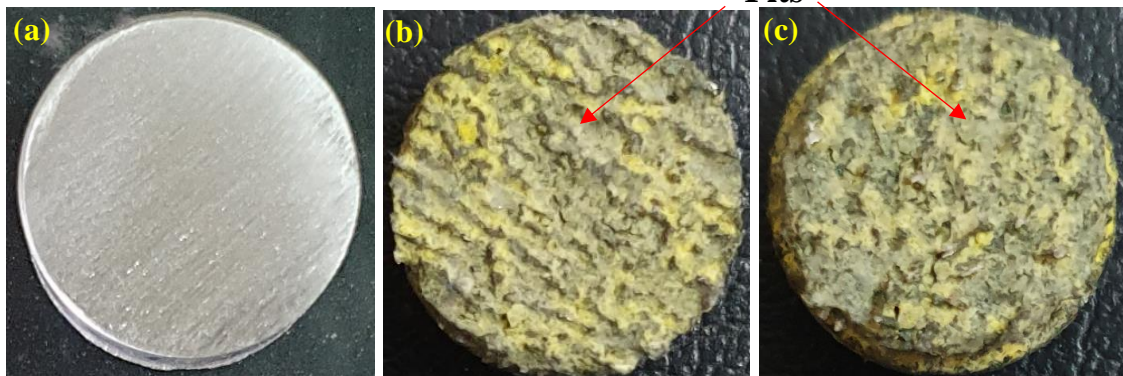


Figure 4.26 CM10 alloy (a) original sample (b) after 6 hrs immersion (c) after 12 hrs immersion in 3.5 wt.% NaCl

Numerous corrosion pits are also observed in the Mg-Cu alloys, and their occurrence becomes more pronounced with increasing copper content. These observations suggest that increased copper content significantly accelerates the corrosion rate, while the presence of manganese helps reduce the severity of corrosion. The Mg_2Cu phase present in these alloys acts as a cathode, facilitating hydrogen (H_2) evolution during corrosion in the presence of an electrolyte such as the NaCl solution used in the study. [95] This Mg_2Cu phase acts as an electrocatalyst, promoting the reduction of H_2 gas at the cathode, leading to the formation of corrosion pits and an overall increase in the corrosion rate, as observed in the Mg-Cu alloys.

Existing literature indicates that certain elements, including Fe, Ni, Cu, and Co, can adversely affect the corrosion resistance of Mg alloys. However, the addition of specific elements such as manganese can help mitigate the detrimental effects caused by these elements. [7, 47] In the case of the Mg-Cu-Mn alloys examined in this study, the beneficial effect of manganese on corrosion resistance is evident, as indicated by the lower corrosion rates observed compared to the Mg-Cu alloys. The EDS analysis of the corrosion product from the CM32 alloy (Fig. 4.27) reveals the presence of both Mg_2Cu and Mn intermetallic phases. These intermetallic phases likely contribute to the reduction of the corrosion rate by providing cathodic protection and modifying the alloy's microstructure to enhance its corrosion resistance. The corrosion product of this alloy appears in powder form, with magnesium dissolved as $Mg(OH)_2$ and hydrogen evolution occurring. [95]

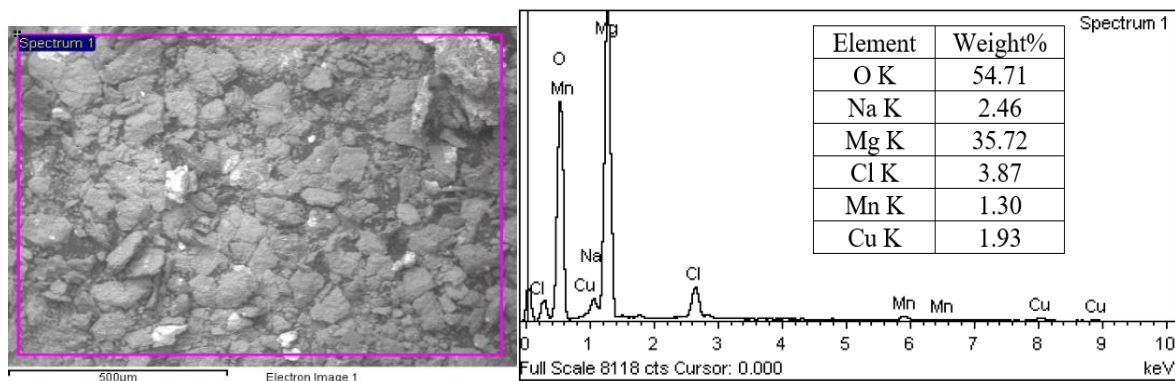


Figure 4.27 EDS analysis of CM32 alloy corrosion product

4.6 Results & Discussion of Part V

Develop and Study the Mg-Ni and Mg-Ni-Mn (NM) Alloys

4.6.1 Chemical Analysis of Developed Systems:

The chemical composition of developed Mg-Ni and Mg-Ni-Mn alloys are shown in table 4.8.

Table 4.8 Chemical analysis of Mg-Ni-Mn alloys

System	Alloy	Ni	Mn	O	Al	Mg
System 17	Mg-0.7Ni	0.72	0.37	4.44	0.17	Balance
System 18	Mg-1.4Ni	1.39	-	3.50	0.31	Balance
System 19	Mg-1.7Ni	1.74	0.45	3.33	-	Balance
System 20	Mg-0.7Ni-2.33Mn	0.72	2.33	3.50	-	Balance
System 21	Mg-1.7Ni-3.15Mn	1.79	3.15	2.96	0.15	Balance
System 22	Mg-2.3Ni-1.96Mn	2.27	1.96	3.34	0.13	Balance

4.6.2 Microstructure Analysis of All Systems by Optical Microscopy and SEM analysis

Figure 4.28 (a) to (f) show the optical microstructures of as-cast Mg-Ni and Mg-Ni-Mn alloys. The microstructure consists of the primary phase of α – Mg and secondary phases. There is a large number of secondary phases observed along the grain boundaries. As per the XRD results and literature survey, the Mg_2Ni phase is present in Mg-Ni alloys. [109, 155–157] As seen in figure 4.28 (a, b, c), with increasing nickel content the shapes, amount and distribution of secondary phases progressively changed. In addition, the grain size is also becoming finer with increasing nickel content. As shown in figure 4.28 (d), manganese addition can refine the grains of Mg-0.7Ni alloy. If more amount of manganese is present in Mg-Ni alloys, grain size becomes coarser and more amount of secondary phases and isolated particles of Mn were observed. (Fig. 1 (e, f)). Table 4.9 provides an overview of the grain sizes observed in all the alloys.

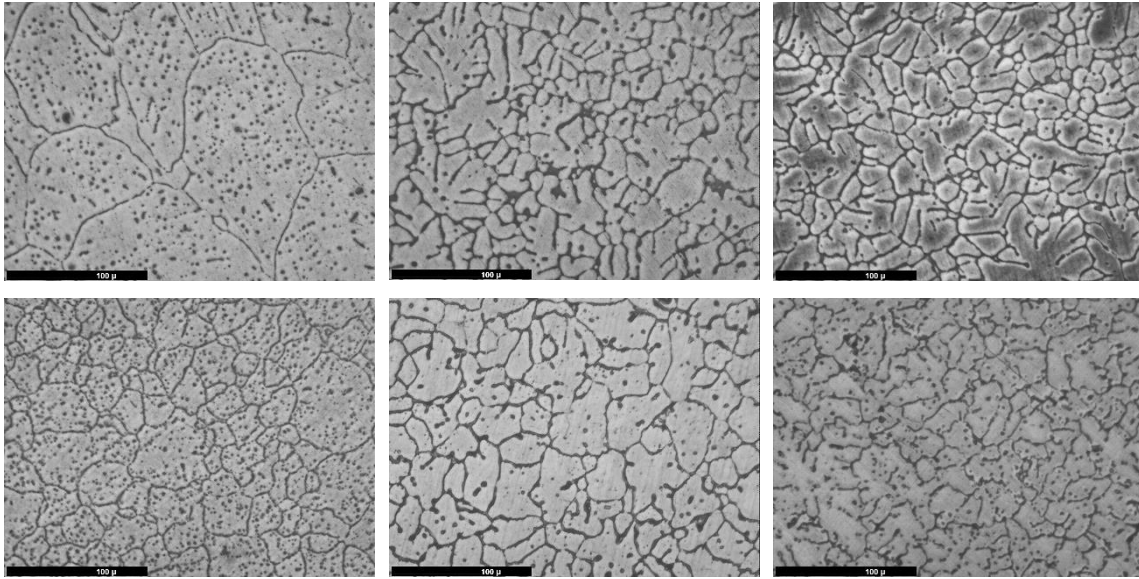


Figure 4.28 Optical Micrographs of the as cast alloys at 200 X (a) Mg-0.7Ni (b) Mg-1.4Ni (c) Mg-1.7Ni (d) Mg-0.7Ni-2.33Mn (e) Mg-1.7Ni-3.15Mn (f) Mg-2.3Ni-1.96Mn

Table 4.9 Grain Size of as-cast Mg-Ni and Mg-Ni-Mn alloys

System	Alloy	Grain Size (μ)
System 17	Mg-0.7Ni	88.02
System 18	Mg-1.4Ni	20.87
System 19	Mg-1.7Ni	18.66
System 20	Mg-0.7Ni-2.33Mn	23.01
System 21	Mg-1.7Ni-3.15Mn	30.67
System 22	Mg-2.3Ni-1.96Mn	21.63

SEM micrographs (550 X) with corresponding EDS analysis of the alloys are given in figure 4.29 and table 4.10, respectively. As shown in figure 4.29, the eutectic morphology of the Mg-Ni is affected by manganese content. By EDS analysis at a particular area, the gray area (marked A, C & D) is rich in the α -Magnesium phase. The bright precipitate at the grain boundaries (marked B, G) of the alloy is rich in Ni. EDS, XRD, and available literature identify this phase as Mg_2Ni . [158] In the microstructure, many isolated particles are observed. These particles are composed of a maximum amount of manganese (marked F).

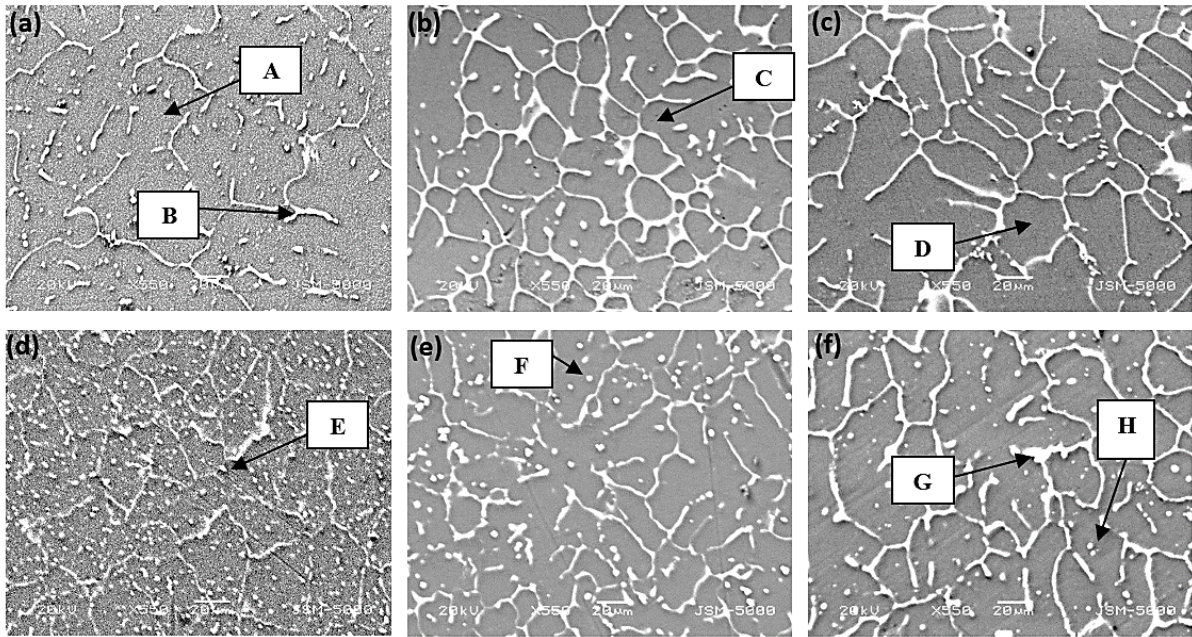


Figure 4.29 SEM Micrographs of the as cast alloys at 550 X (a) Mg-0.7Ni (b) Mg-1.4Ni (c) Mg-1.7Ni (d) Mg-0.7Ni-2.33Mn (e) Mg-1.7Ni-3.15Mn (f) Mg-2.3Ni-1.96Mn

Table 4.10 Chemical compositions of as-cast Mg-Ni and Mg-Ni-Mn alloys (weight %)

Location (point)	Mg	Ni	Mn	O	Other
Figure 24 (a), A	94.30	0.72	0.37	4.44	0.17
Figure 24 (b), B	78.92	12.30	0.38	7.40	1.01
Figure 24 (c), C	94.80	1.39	-	3.50	0.31
Figure 24 (c), D	94.48	1.74	0.45	3.33	-
Figure 24 (d), E	83.43	1.52	11.87	2.61	0.58
Figure 24 (e), F	22.06	3.15	69.15	4.37	1.27
Figure 24 (f), G	76.29	15.09	6.11	2.51	-
Figure 24 (f), H	82.43	1.45	12.12	2.96	1.04

The composition of phases in Mg-Ni and Mg-Ni-Mn alloys is determined by XRD and the results are shown in figure 4.30. It can be observed that the main phases of Mg-Ni alloys are α -Mg and Mg_2Ni . After the addition of manganese, a new Mn phase is observed. The phases α -Mg and Mg_2Ni have a hexagonal structure and Mn has a cubic structure. It is seen that the number of Mg_2Ni peaks increases with the increasing Ni content.

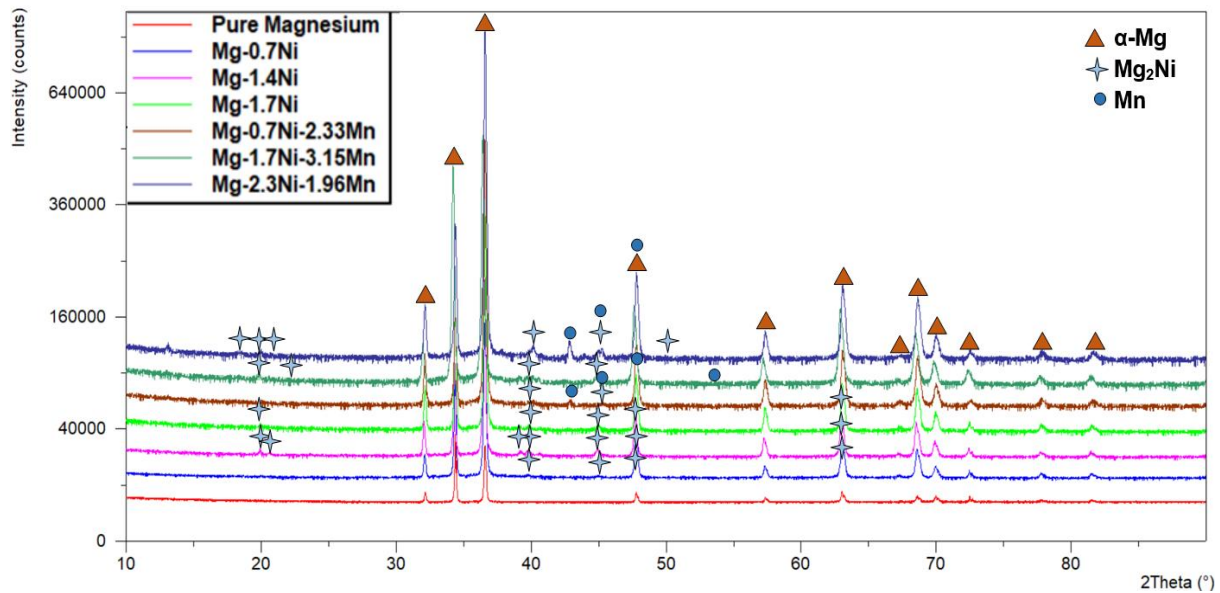


Figure 4.30 XRD patterns of (a) Mg-0.7Ni (b) Mg-1.4Ni (c) Mg-1.7Ni (d) Mg-0.7Ni-2.33Mn (e) Mg-1.7Ni-3.15Mn (f) Mg-2.3Ni-1.96Mn alloy

4.6.3 Mechanical Properties

Figure 4.31 shows the ultimate tensile strength, hardness, and % elongation results for all developed alloys. According to the conventional Hall-Petch relationship, which relies on the dislocation accumulation theory, the strength of a material increases as its grain size decreases. [159, 160] As discussed in section 4.6.2, the presence of nickel and manganese in the alloys refines the grain structure of pure magnesium. As a result, the alloys containing Ni and Mn exhibit higher ultimate tensile strength and hardness values compared to pure magnesium. The ultimate tensile strength of more than 1% nickel-containing alloy is around 160 MPa. Compared to previous work in Refs [112], UTS of Mg-3%Ni alloy is 124.4 MPa and elongation is 1.16 %, significant improvement is observed here.

As discussed in 4.6.2, grain is more refined in Mg-1.4Ni alloy compared to Mg-0.7Ni alloy. So, there is a great improvement in UTS, and the Hardness value is seen in Mg-1.4Ni alloy. By adding Mn, no significant changes are observed in the UTS value. Vicker's hardness of Mg-Ni and Mg-Ni-Mn alloys lying between 47 to 59 HV. Maximum hardness is achieved in Mg-2.3Ni-1.96Mn alloy i.e. 59 HV. There is a negligible difference is observed in % Elongation of different alloys.

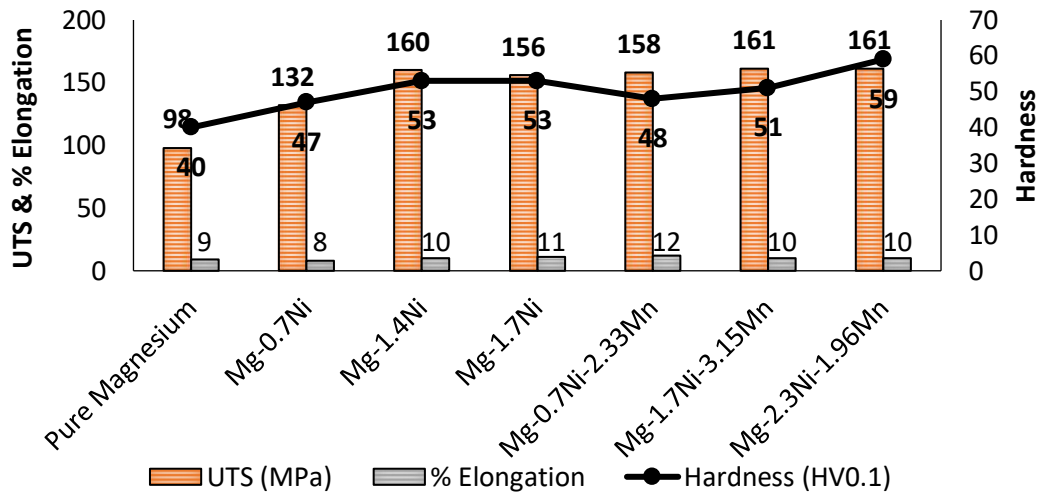


Figure 4.31 Room temperature mechanical properties of as-cast Mg-Ni and Mg-Ni-Mn alloys

4.6.4 Corrosion Behaviour

The density of an alloy depends on the presence of different metal elements. According to literature sources [47, 145, 161], the densities of pure magnesium, nickel, and manganese are reported to be 1.738 g/cc, 8.902 g/cc, and 7.47 g/cc, respectively. It is known that the presence of nickel and manganese increases the density of pure magnesium [162]. In the case of Mg-Ni and Mg-Ni-Mn alloys, the densities range from 1.743 g/cc to 1.785 g/cc, as shown in figure 4.32.

Figure 4.33 presents the images of the Mg-Ni and Mg-Ni-Mn alloys before and after immersion in a 3.5 wt.% NaCl solution for 1.5 hours and 2 hours. Upon immersion, a vigorous reaction was observed in all alloys. The pictures in figure 4.33 demonstrate that the thickness and diameter of the Mg-Ni and Mg-Ni-Mn alloys decrease after immersion. The corrosion rates of all alloys are provided in table 3, revealing that the presence of nickel significantly increases the corrosion rate of magnesium. Among the alloys, the Mg-1.4Ni alloy exhibited the highest corrosion rate, reaching 321884 mpy.

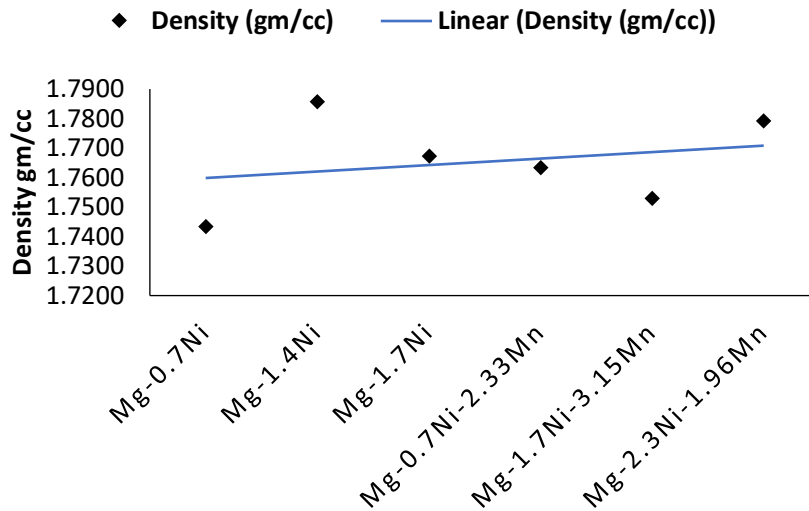


Figure 4.32 Density of Mg-Ni and Mg-Ni-Mn alloys

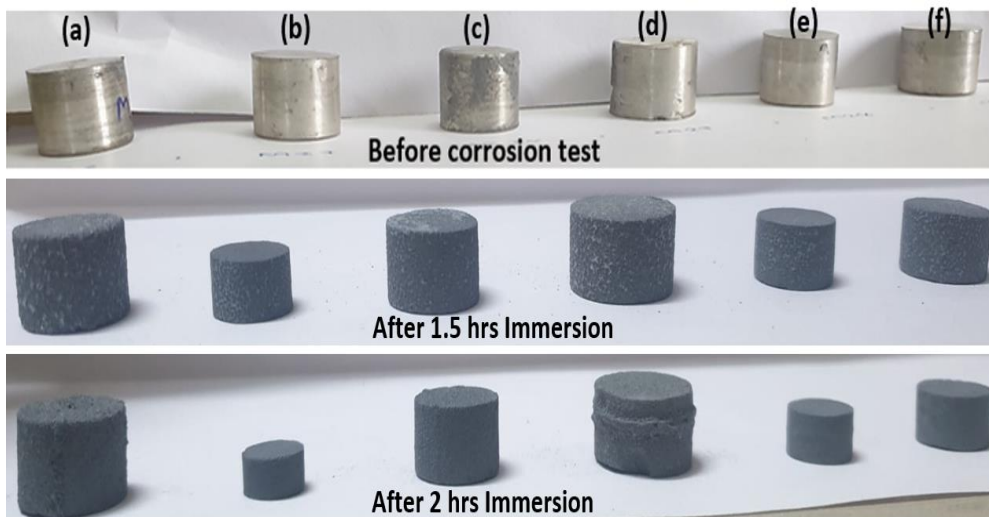
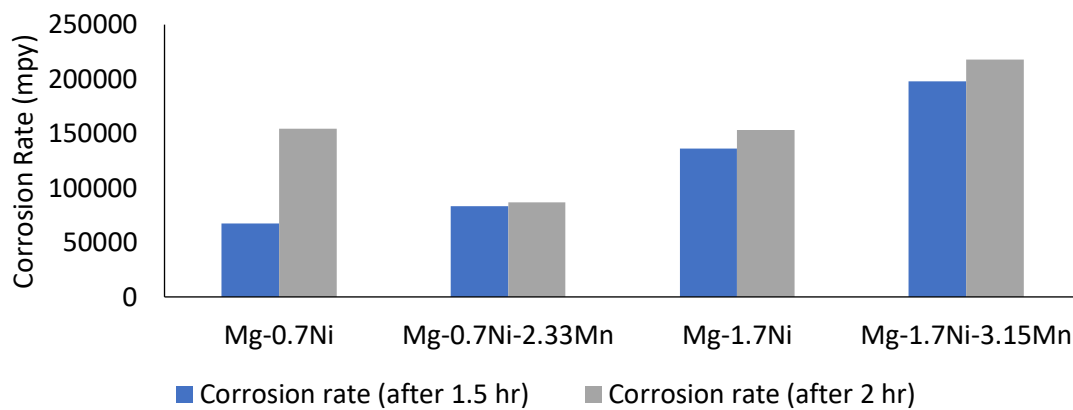
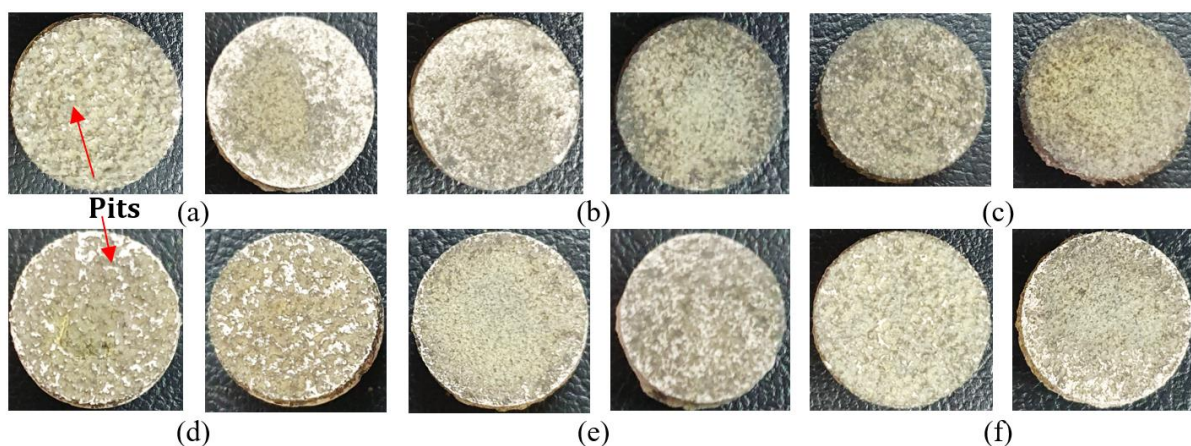


Figure 4.33 Photographs of the (a) Mg-0.7Ni (b) Mg-1.4Ni (c) Mg-1.7Ni (d) Mg-0.7Ni-2.33Mn (e) Mg-1.7Ni-3.15Mn (f) Mg-2.3Ni-1.96Mn alloy before and after corrosion test

In many magnesium alloys, the addition of manganese has been known to improve corrosion resistance. However, in the case of the Mg-0.7Ni-2.33Mn alloy, the corrosion rate is higher compared to the Mg-0.7Ni alloy. Figure 4.34 illustrates that the corrosion rate of the developed alloys increases with time. Numerous corrosion pits are observed on the alloy surfaces (figure 4.35 & 4.36), and their number increases with higher nickel content. Surprisingly, the presence of manganese appears to have an adverse effect on the corrosion rate, as Mn-containing Mg-Ni alloys exhibit a higher corrosion rate compared to Mg-Ni alloys without manganese.

Table 4.11 Corrosion rates (mpy) after 1.5 hrs and 2 hrs immersion in 3.5 wt. % NaCl of Mg-Ni alloys Mg-Ni-Mn alloys

Alloy	Corrosion rate (mpy) (After 1.5 hr)	Corrosion rate (mpy) (After 2 hr)
Mg-0.7Ni	67628	154642
Mg-1.4Ni	321884	311720
Mg-1.7Ni	135928	153215
Mg-0.7Ni-2.33Mn	83133	86917
Mg-1.7Ni-3.15Mn	197830	217978
Mg-2.3Ni-1.96Mn	100975	234362

**Figure 4.34** Corrosion rates of Mg-0.7Ni, Mg-0.7Ni-2.33Mn, Mg-1.7Ni and Mg-1.7Ni-2.15Mn alloy**Figure 4.35** Photographs of the (a) Mg-0.7Ni (b) Mg-1.4Ni (c) Mg-1.7Ni (d) Mg-0.7Ni-2.33Mn (e) Mg-1.7Ni-3.15Mn (f) Mg-2.3Ni-1.96Mn after 1.5 hrs and 2 hrs immersion in 3.5wt. % NaCl after cleaning

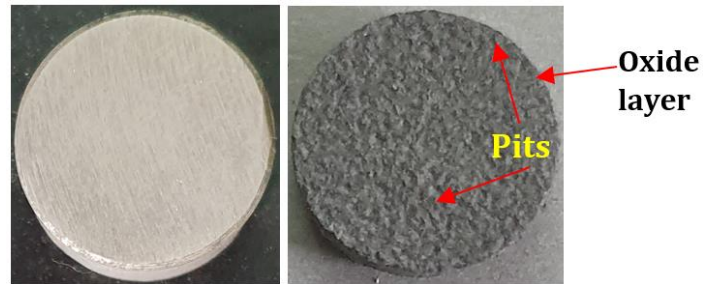


Figure 4.36 Mg-1.4Ni alloy (a) before (b) after 2 hrs immersion in 3.5wt. % NaCl (without cleaning)

It is commonly documented that the corrosion resistance of magnesium alloys is often related to grain refinement. [163–165] However, in this study, it is observed that the corrosion rate increases with decreasing grain size. The Mg_2Ni secondary phase acts as a cathode and accelerates the corrosion of the magnesium matrix. The corrosion product of these alloys is in powder form. Both literature references and EDS analysis (figure 4.37) confirm that magnesium is dissolved in the form of MgO , $Mg(OH)_2$, and H_2 gas is evolved. [95, 157] The presence of Mg, Ni and Mn in the corrosion product can also be confirmed through EDS analysis.

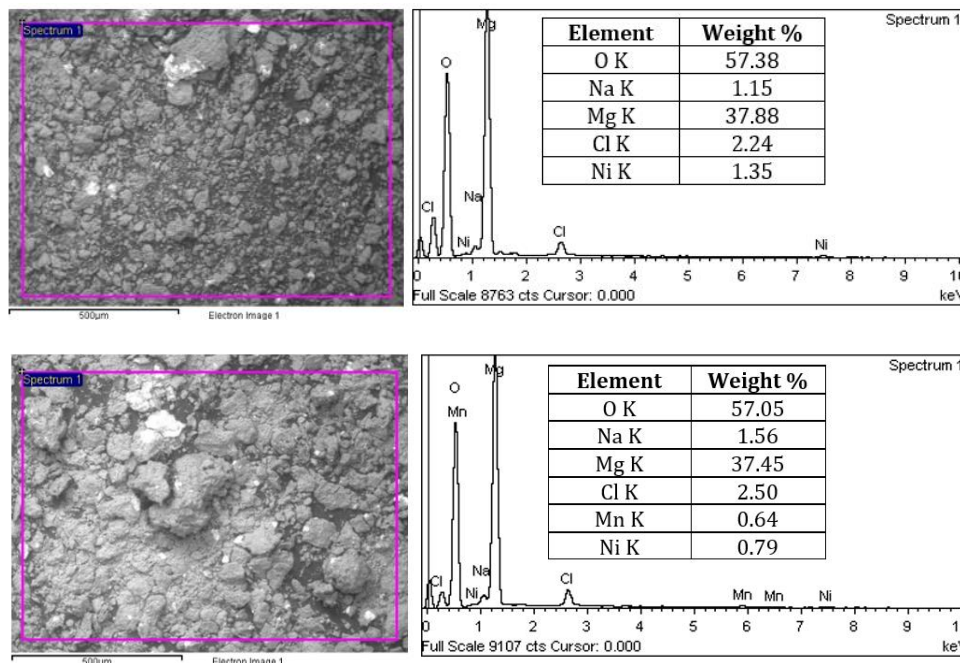


Figure 4.37 EDS analysis of (a) Mg-1.4Ni (b) Mg-1.7Ni-3.15Mn alloy corrosion product